

Operational Aerosol Observations (AEROBS) from AVHRR/3 On Board NOAA-KLM Satellites

ALEXANDER IGNATOV*

NOAA/NESDIS/Office of Research and Applications, Camp Springs, Maryland

JOHN SAPPER

NOAA/NESDIS/Office of Satellite Data Processing and Distribution, Suitland, Maryland

STEPHEN COX

Science and Technology Corporation, and NOAA/NESDIS/Environmental Product Systems, Suitland, Maryland

ISTVAN LASZLO AND NICHOLAS R. NALLI

NOAA/NESDIS/Office of Research and Applications, Camp Springs, Maryland

KATHERINE B. KIDWELL

NOAA/NESDIS/Office of Satellite Data Processing and Distribution, Suitland, Maryland

(Manuscript received 22 April 2003, in final form 22 July 2003)

ABSTRACT

Since 1988, the National Oceanic and Atmospheric Administration (NOAA) has provided operational aerosol observations (AEROBS) from the Advanced Very High Resolution Radiometer (AVHRR/2) on board the afternoon NOAA satellites [nominal equator crossing time, (EXT) ~ 1330]. Aerosol optical depth (AOD) has been retrieved over oceans from channel 1 of AVHRR/2 on board *NOAA-11* (1988–94) and *-14* (1995–2000) using the first- and second-generation algorithms, respectively. With the launch of the NOAA-KLM series of satellites, in particular *NOAA-16* (L) in September 2000 (EXT ~ 1400), and *NOAA-17* (M) in June 2002 (EXT ~ 1000), an extended and improved third-generation algorithm was enabled. Like its predecessors, this algorithm continues to employ a single-channel methodology, by which all parameters in the retrieval algorithm (excluding AOD) are set globally as nonvariables. But now, in addition to AOD from channel 1, τ_1 ($\lambda_1 = 0.63 \mu\text{m}$), the algorithm also retrieves τ_2 and τ_3 in AVHRR/3 channels 2 ($\lambda_2 = 0.83 \mu\text{m}$) and 3A ($\lambda_3 = 1.61 \mu\text{m}$). The retrievals are made with more accurate and flexible, satellite- and channel-specific lookup tables generated with the Second Simulation of the Satellite Signal in the Solar Spectrum (6S) radiative transfer code. From pairs of τ_i and τ_j , the Ångström exponent (AE) parameters can then be determined as $\alpha_{ij} = -\ln(\tau_i/\tau_j)/\ln(\lambda_i/\lambda_j)$.

This paper describes the AEROBS processing and gives examples of aerosol products, along with a preliminary diagnostics of their quality using some of the previously developed self-consistency checks. Interconsistency between the *NOAA-16* and *-17* aerosol retrievals is also checked. The AODs are largely coherent but distorted by the AVHRR calibration uncertainties, and subject to noise and outliers. These τ errors, unavoidable in real-time AVHRR processing, severely impact the derived AE, demonstrating a fundamental instability in estimating the aerosol model under typical maritime conditions from AVHRR. Consequently, it is concluded that the robust single-channel retrievals should be continued in the AEROBS operations in the KLM era. The more sophisticated multichannel techniques may be tested while reprocessing historical AVHRR data, only after the data quality issues have been resolved (viz., calibration uncertainties constrained, outliers removed, and noise suppressed by spatial averaging).

* CIRA Visiting Scientist.

Corresponding author address: Dr. Alex Ignatov, E/RA1, NOAA, WWBG, Rm. 7113, 5200 Auth Rd., Camp Springs, MD 20746-4304.
E-mail: Alex.Ignatov@noaa.gov

1. Introduction and background

Operational aerosol observations (AEROBS) obtained from the Advanced Very High Resolution Radiometer (AVHRR) on board the National Oceanic and Atmospheric Administration (NOAA) polar-orbiting satellites continue to be a valuable aerosol data product developed and maintained by the NOAA/National Environmental Satellite, Data, and Information Service (NESDIS). Aerosol optical depth (AOD) has been retrieved from channel 1 ($\lambda_1 = 0.63 \mu\text{m}$) of AVHRR/2 on board *NOAA-11* (1988–94) and *-14* (1995–2000) over oceans in real time, using the first- (Rao et al. 1989) and second- (Stowe et al. 1997) generation algorithms, respectively. The second-generation algorithm has been also used to reprocess, retrospectively, the *NOAA-7*, *-9*, *-11*, and *-14* data within the Pathfinder Atmosphere (PATMOS) project (Stowe et al. 2002).¹ Both the *NOAA-11* and *-14* operational AEROBS files, and the current version of PATMOS, report the AOD obtained from channel 1, τ_1 . Single-channel retrievals from channel 2 ($0.83 \mu\text{m}$) of the AVHRR/2 on board *NOAA-14* (Stowe et al. 1997), and from the $1.61\text{-}\mu\text{m}$ channel of the Visible and Infrared Scanner (VIRS) on board the Tropical Rainfall Measuring Mission (TRMM) satellite (launched November 1998; Ignatov and Stowe 2000), have both been tested offline. With the launch of the NOAA-KLM series of satellites [in particular, *NOAA-16* (L) and *NOAA-17* (M)], transition to an improved operational third-generation algorithm has been achieved.

The first- and second-generation algorithms were lacking a number of important capabilities for remote sensing of aerosol, chiefly because they were based on the Dave (1973) code originally developed for ozone applications. In particular, the specular component of reflection from the ocean surface was not accounted for, and the aerosol modeling was inflexible. Accurate integration of the top-of-the-atmosphere (TOA) radiances over the wide AVHRR spectral filters was not straightforward with the monochromatic Dave code. Absorption by all optically active gases in the AVHRR channels, except ozone, was missing from the original version of the code and, therefore, had been added ad hoc. Often, this information was not up to date.

Ignatov and Stowe (2002a) tested the newer Second Simulation of the Satellite Signal in the Solar Spectrum (6S; Vermote et al. 1997) radiative transfer model (RTM) and found it preferable to the outdated Dave

RTM. The specular surface reflectance is now characterized based upon the Cox and Munk (1954) model, thus constituting a significant improvement over the previously used “diffuse glint” correction based on a single-scattering approximation that was added to the Dave code (Ignatov et al. 1995). A wide choice of aerosol geophysical and microphysical (up to four lognormal modes) models is available. Rayleigh scattering and gaseous absorption are now explicitly calculated within 6S by an accurate integration over the satellite sensor-specific spectral response functions. This more rigorous approach is preferable to the previous approach of using one set of gaseous and Rayleigh optical depths for all similar channels on all AVHRR sensors. Accounting for the shifts in the spectral responses of the channels ensures consistency in the optical depths retrieved from different AVHRR instruments (in particular on board *NOAA-16* and *-17*), and reduces the resulting artificial discontinuities between the satellites. Generating consistent single channel lookup tables (LUTs) for the spectral channels of various sensors on board different platforms (such as the new $1.61\text{-}\mu\text{m}$ channels on AVHRR/3 and TRMM/VIRS) is now a relatively simple and straightforward task. The retrievals from a variety of AVHRR-like sensors are conveniently reported at the standard reference centroid wavelengths (i.e., $\lambda_1 = 0.630$, $\lambda_2 = 0.830$, or $\lambda_3 = 1.610 \mu\text{m}$), making data from different platforms directly comparable.

In the third-generation algorithm, the channel-specific surface diffuse component reflectance is assumed to be globally nonvariable, whereas the surface specular component reflectance is specified assuming a fixed wind speed. Concentrations of absorbing gases (ozone in channel 1 and water vapor in channel 2), and surface pressure (Rayleigh optical depth), continue to be specified from the midlatitude summer standard atmosphere. The 6S RTM allows for accurate characterization of all these factors, but unfortunately global and seasonal distributions of wind speed, chlorophyll concentration, gaseous concentrations and surface pressure are not currently available in either AEROBS or PATMOS data. Work is under way to include this ancillary data, at which time they can be incorporated into the retrievals. In the meantime, the fixed surface diffuse reflectance and aerosol microphysics used in the second-generation algorithm, have been reexamined, and no evidence was found to warrant their adjustment at this time (Ignatov and Stowe 2002a).

The third-generation aerosol algorithm is an evolutionary improvement and extension of the former NESDIS first- and second-generation operational aerosol retrievals (Ignatov and Stowe 2002a). After extensive evaluation with AEROBS data of *NOAA-14* (Ignatov and Stowe 2002b), PATMOS–Buoy matchup data of *NOAA-11* and *-14* (Ignatov and Nalli 2002), and TRMM/VIRS data (A. Ignatov et al. 2003, unpublished manuscript), the third-generation algorithm has been im-

¹ The difference between the *historical* PATMOS and the *operational* AEROBS aerosols is twofold. First, the AVHRR calibration in AEROBS is in real time (often prelaunch), whereas PATMOS reprocessing is based on improved postlaunch coefficients. Sampling and cloud screening are also different (Ignatov and Nalli 2002). Effort is under way to unify the two procedures (A. K. Heidinger, A. Jelenak, and J. Sapper 2003, unpublished manuscript). Both the historical PATMOS, and real-time AEROBS aerosol products are available from the NOAA Satellite Active Archive Web page (www.saa.noaa.gov).

plemented into AEROBS operations with the launch of *NOAA-16* (L) in September 2000, followed by *NOAA-17* (M) in June 2002.

In the sections that follow, we 1) describe the current NOAA operational KLM AEROBS processing, 2) provide some examples of aerosol products, and 3) conduct a preliminary examination of their quality. The primary conclusion of this work is that in the NOAA operations, single-channel retrievals are preferable over multichannel retrievals because they are more robust to the AVHRR uncertainties. The single-channel product should thus be continued as long as AVHRR reflectance channels remain noncalibrated on board (viz., 10–15 yr beyond the present), serving two major objectives: 1) to reliably monitor spatiotemporal evolutions of aerosol fields over global oceans in real time, and 2) to monitor vicariously the radiometric performance of AVHRR/3 individual channels.

2. NOAA-KLM platforms and AVHRR/3 instrument: Implications for aerosol retrievals

A new series of NOAA Polar Operational Environmental Satellites (POESs) commenced with the launch of *NOAA-15* (K) in March 1998, followed by *NOAA-16* (L) in September 2000, and *NOAA-17* (M) in June 2002 (Goodrum et al. 2003). Although formally a continuation of the *TIROS-N* and advanced *TIROS-N* (ATN) series of satellites, the NOAA-KLM satellites represent a significant evolution and open up a new era of improved environmental monitoring in support of NOAA missions. In particular, for aerosol retrievals, two new features are important. First, the KLM orbital configuration differs somewhat from that of the previous *TIROS-N*/ATN scheme, which will affect aerosol retrievals through the changed illumination regime. Also, the AVHRR/3 flown on board KLM is a greatly improved edition over its predecessor, AVHRR/2. These two changes are considered below, in sequence, along with their implications for aerosol retrievals. These are followed by a brief outlook toward the future of NOAA aerosol operations in an attempt to put the KLM into a historical context.

a. NOAA orbital configuration²

The orbits for the NOAA polar-orbiting satellites have been carefully chosen to achieve a globally uniform earth coverage by cross-scanning instruments on board, such as the AVHRR. A few measurements a day distributed more or less uniformly in time are needed. An additional requirement is that each measurement be

made at the same local time (LT) day after day, to provide for consistent scene illumination (for AVHRR solar reflectance channels) or segment of diurnal cycle (for the thermal infrared channels).

Given these constraints, the observing, acquisition, and ground control conflicts have been minimized by placing NOAA satellites in two types of near-circular (mean heights ~ 870 and ~ 833 km), sun-synchronous (inclination $\sim 99^\circ$) orbits, whose planes are about 90° (6 h) apart along the approximate north–south axis. The “afternoon” satellites prior to *NOAA-16* have been launched in an “ascending” (northbound) orbit [local equator crossing time (EXT) ~ 1330]. This orbit “descends” back from north to south on the dark side of the earth at EXT ~ 0130 . The “morning” satellites (except *NOAA-17*) have been launched in a descending (southbound) orbit with an EXT ~ 0730 . The ascending (northbound) node passes on the local evening (EXT ~ 1930)³.

Given the nominal EXTs, the illumination conditions are favorable for aerosol retrievals from P.M. orbits of the afternoon satellites only (the morning satellites observe the earth at dark from both A.M. and P.M. orbits). Although the 1330/0130 and 0730/1930 are the target overpass times at launch, the actual EXTs change during satellite lifetime. Figure 1 shows time series of the EXT for the six earliest NOAA satellites, of which only two (*NOAA-16* and *-17*, as of time of this writing) are operational while all others are in a standby mode (i.e., serving as a backup for an operational platform). The afternoon satellites tend to drift toward later in the afternoon, whereas the morning satellites shift toward earlier hours. This results in a complex EXT pattern that makes the afternoon and morning nomenclature even more confusing. For instance, the afternoon *NOAA-11* (EXT $\sim 0130/1330$ at launch) during its 15 yr in orbit made it all the way through the morning mode (EXT $\sim 0730/1930$ at launch) to an almost afternoon regime again. Its ascending (northbound) orbit now passes at EXT ~ 2300 , and the descending (southbound) orbit occurs at EXT ~ 1100 . This development would make the current *NOAA-11* 1100 orbit suitable for aerosol retrievals again, if its AVHRR/2 had not failed back in 1999. The other afternoon satellite, *NOAA-14*, during its ~ 8 yr lifetime has moved into an almost morning orbit with an EXT $\sim 0700/1900$, which is not useable for aerosol retrievals. Additionally, its AVHRR/2 scan motor spiked

² This section provides the minimum information needed to understand the aerosol retrievals from NOAA–AVHRR. It borrows heavily from Rao et al. (1990), Kidwell (1998), and Goodrum et al. (2003). The reader is advised to check these references for more detail.

³ Note that the definitions of the “morning” and “afternoon” platforms, widely used in the community, are rather confusing. In particular, either platform has *both* an A.M. and P.M. pass (unlike its name may suggest). Furthermore, the A.M. pass of a morning platform occurs while on a descending node, whereas the P.M. pass of an afternoon platform is on an ascending node. The ascending nodes occur in the afternoon for both platforms, at 1330 and 1930, and likewise, the descending nodes occur in the morning, at 0130 and 0730. Moreover, the local EXT changes during satellite lifetime as discussed below. Note that whatever evolution to the EXT may occur during the lifetime of a platform, its “morning” or “afternoon” attribute designated at launch remains unchanged.

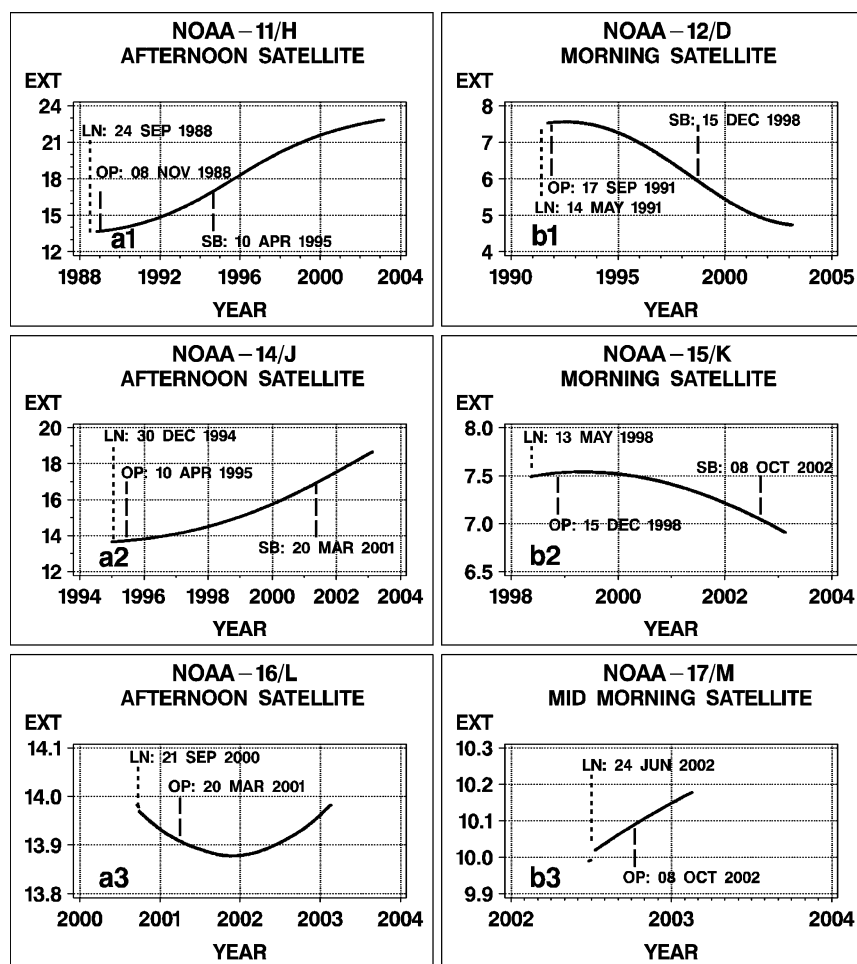


FIG. 1. EXT (in h) for the six NOAA platforms currently in orbit (ascending–northbound node for afternoon, and descending–southbound for morning platforms). Satellite dates: LN, launch; OP, became operational; and SB, put into standby mode (serves as a backup for an operational platform). Note that the OP/SB dates refer to platform, and may not necessarily be representative of the AVHRR instrument performance. NOAA is currently preparing a full log of all the AVHRR instruments' performance, which will become available online in the near future.

on 18 October 2001. The *NOAA-12*, after ~ 12 yr in orbit, has slipped back in time to an early morning/late afternoon orbit with an EXT $\sim 0430/1630$. The illumination from its P.M. orbit is marginal for aerosol retrievals, and the AVHRR/2 on *NOAA-12* is still functioning well. It is thus clear that out of the four backup platforms currently in orbit, only *NOAA-12* can serve as a replacement for aerosol retrievals should either *NOAA-16* or *-17* fail.

Figure 1b2 shows the EXT for the morning *NOAA-15* (K) satellite, the first in the KLM series. During 5 yr in orbit, its EXT lost ~ 40 min, and currently it passes at $\sim 0650/1650$. Both of these orbits are too dark to be used for aerosol retrievals. Additionally, the AVHRR/3 on board *NOAA-15* has degraded substantially. The *NOAA-16* (L) was launched into a modified afternoon orbit with an EXT ~ 1400 (northbound/ascending node). Figure 1a3 shows that its EXT did not change much

after ~ 3 yr in orbit, thanks to a special effort to stabilize the KLM orbits. The *NOAA-17* (M) was put into an unusual midmorning orbit with an EXT ~ 1000 (southbound/descending node). This means that for the first time in NOAA operations, the morning platform is useable for aerosol retrievals. Note also that the new NOAA orbits closely resemble those of the *Terra* (EXT ~ 1030) and *Aqua* (EXT ~ 1330) platforms carrying the Moderate Resolution Imaging Spectroradiometer (MODIS) instrument, which is widely used for aerosol retrievals (e.g., Kaufman et al. 2000; Remer et al. 2002).

Aerosol retrievals are currently obtained from both operational platforms *NOAA-16* and *-17*. Figure 2 shows histograms of the respective LTs of aerosol observations (calculated as $LT = UTC - \text{longitude}/15^\circ$, where UTC is coordinated universal time, and longitude is defined in the range from -180° to 180°). The LTs tend to be generally clustered around the EXT ~ 1400 for *NOAA-*

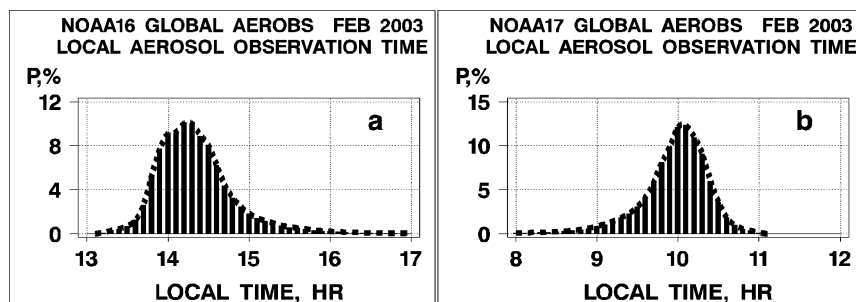


FIG. 2. Local solar time of aerosol observations from the (a) afternoon *NOAA-16* (EXT ~ 1400) and (b) midmorning *NOAA-17* (EXT ~ 1000) platforms.

16, and EXT ~ 1000 for *NOAA-17*, but the actual aerosol observations may be taken anywhere within up to a few hours around those times. The reason for that is twofold. First, the local overpass time changes systematically with latitude, due to earth rotation and orbit inclination. Additionally, the AVHRR scans cross-track up to more than a 1000 km off nadir (view angle in the AEROS files is restricted to 60° ; note also that the aerosol retrievals are made on the antisolar side of the orbit only). Figure 2 thus suggests that any time referencing for the aerosol retrievals using only the EXT might not be sufficient.

b. AVHRR/3

The AVHRR/3 is an improved imaging instrument with the overall sensor design upgraded from AVHRR/2 (Goodrum et al. 2003). In particular, a larger external sun shield has been added to the AVHRR/3 scan motor housing to reduce sunlight impingement and associated calibration problems that have been occasionally observed during some prior missions.

A third solar reflectance channel centered at $\lambda_3 = 1.61 \mu\text{m}$ was added to the previous two centered at $\lambda_1 = 0.63$ and $\lambda_2 = 0.83 \mu\text{m}$, for a better snow-ice discrimination and aerosol retrievals. The new channel is designated 3A since it is time shared with the $3.7\text{-}\mu\text{m}$ channel (previously channel 3, now called 3B). In the past, channel 3 transmitted $3.7\text{-}\mu\text{m}$ data from all NOAA platforms full time. However, on *NOAA-16* and *-17*, channel 3B is “on” (and hence 3A is “off”) on the dark side of the earth, whereas on the sunlit part of the orbit these positions are switched over automatically to a 3A on–3B off mode. There has been a strong demand from the fire and cloud detection communities to have the 3B on during daytime on the afternoon platform. A compromise has been achieved between the two groups of users, by which the transmission of 3A data had been discontinued from *NOAA-16* on 1 May 2003 but continues from *NOAA-17*. This scenario will remain in place as long as the two current satellites operate normally. The one-satellite contingency scenario is yet to be formulated.

Another feature of the AVHRR/3 that is important

for aerosol retrievals is a refined sensitivity at low radiance levels. A 10-bit digitization (from 0 to 1023 counts) remained unchanged on the KLM series. But on the AVHRR/2 it had been used to uniformly represent the 0%–100% albedo range, whereas on AVHRR/3 channels 1 and 2, only the first half of the dynamic range (0–500 counts) represents 0%–25% albedo, making the AVHRR/3 count worth $\sim 1/2$ that on AVHRR/2. In channel 3A, where the signal over ocean is even lower compared to the visible–near-IR, the first half of the dynamic range (from 0 to 500 counts) spans from 0% to 12.5% albedo, making the 3A count worth $\sim 1/4$ ($\sim 1/2$) that in channels 1 and 2 of AVHRR/2 (AVHRR/3). This improvement is achieved through the use of the concept of dual slope, or split gain.

The AVHRR/3 solar reflectance channels 1, 2, and 3A remain noncalibrated on board. The accuracy of the vicarious calibration is often cited to be within $\pm 5\%$ for AVHRR/2 channels 1 and 2 [e.g., Rao and Chen (1996, 1999) and Rossow and Schiffer (1999)]; see also a review of AVHRR/2 calibration results in Ignatov (2002)], although the actual accuracy may be worse. Vicarious calibration techniques customarily rely on a few stable targets on earth to be used as a reference, such as the Libyan Desert (Rao and Chen 1996, 1999), and Antarctic or Greenland ice sheets (Tahnk and Coakley 2001a,b). Both of these targets tend to fall within the high-gain radiance of AVHRR/3, and it is still not fully clear at this time how to calibrate the low gain. Heidinger et al. (2002) merged two *NOAA-16* and *Terra* orbits (17 May and 5 July 2001) to calibrate the AVHRR/3 using collocated MODIS reflectances in spectrally proximate bands as a reference. For NOAA operations, this technique should be employed with both operational NOAA platforms (*NOAA-16* with *Aqua*, and *NOAA-17* with *Terra*). Furthermore, it should be run continuously over time, as the AVHRR gains are known to degrade in orbit. The accuracy of the MODIS-based calibration of AVHRR/3 is yet to be determined, but obviously depends upon the MODIS standard itself, and on the procedure to transfer it to AVHRR. Recall that no previous estimates of calibration accuracy were available for channel 3A as this channel is new to AVHRR/3.

c. Beyond KLM

The KLM series will be succeeded by the Initial Joint Polar-Orbiting Operational Satellite System (IJPS). The IJPS is a cooperative effort of NOAA and the European Organization for the Exploitation of Meteorological Satellites (EUMETSAT), each of which will contribute a few satellites with AVHRR/3 on board. NOAA will launch NOAA-N in June 2004, and NOAA-N' in March 2008, and EUMETSAT is responsible for the launch of three Meteorological Operational (METOP-1, -2) satellites in 2005, 2010, and 2014, respectively. More information on the IJPS project can be found by referencing the IJPS Web site (<http://discovery.osd.noaa.gov/IJPS/index.htm>). The NOAA-N and -N' satellites will be launched in the afternoon orbit (EXT ~ 1400 , ascending node), while the METOP-1 and -2 platforms will be placed in the midmorning orbit (EXT ~ 0930 , descending node).

After NOAA-N', the current NOAA satellites will be gradually superseded by the National Polar Orbiting Environmental Satellite System (NPOESS) series, which will carry a new Visible Infrared Imager Radiometer Suite (VIIRS) instrument. The VIIRS will have more reflectance channels that cover a wider spectral interval and are better radiometrically characterized compared to the AVHRR/3. Most notably, the VIIRS will be calibrated on board. This would enable aerosol retrievals from the NPOESS/VIIRS with a simultaneous-solution, multichannel algorithm, currently under development by an NPOESS contractor, the Raytheon Systems Company. The NPOESS Preparatory Project (NPP) satellite is scheduled for launch in December 2005. During NPOESS, three satellites will be operated at once, with EXT ~ 1330 , ~ 1730 , and ~ 2130 while in ascending node (EXT ~ 0130 , ~ 0530 , and ~ 0930 , respectively, while in descending node). The EXT ~ 1330 and ~ 0930 (and possibly ~ 1730) orbits would be used for aerosol retrievals. More information can be found at the Web site of the Integrated Program Office (IPO), which manages the NPOESS project (<http://www.ipo.noaa.gov>).

3. AEROBS processing

In NOAA/NESDIS operations, aerosol retrievals are done within the so-called aerosol observation (AEROBS) system. Historically, AEROBS is a part of the sea surface temperature (SST) observation (SSTOBS) processing system, which in turn is but a small part of a system developed over years of NESDIS operations. Below, we give only a brief overview of this system as relevant to the aerosol retrievals.

The AEROBS/SSTOBS product resides on the NESDIS Central Environmental Monitoring Satellite Computer System (CEMSCS) as a rotating file, which at each given point in time contains all aerosol/SST retrievals during the last 8 days (approximately representing the full repeat cycle of a NOAA satellite). The

file is renewed automatically 4 times a day, around 0100, 0700, 1300, and 1800 eastern standard time. Since NOAA-17 became operational in October 2002, a second AEROBS file has been processed in addition to NOAA-16.

The AEROBS/SSTOBS software receives level 1b data as input and processes them by "target." A target is defined as an 11×11 array of AVHRR 4-km global area coverage (GAC) fields of view (FOVs) centered on the FOVs of the High-Resolution Infrared Radiation Sounder (HIRS), an instrument flown synergetically alongside AVHRR on board NOAA satellites (Kidwell 1998; Goodrum et al. 2003). The HIRS FOV targets overlap by 4 or 5 AVHRR GAC FOVs out of 121, depending on the collocation. Approximately 60 000 targets per orbit, 14 orbits per day, are processed.

First, the quality control (QC) flags of the target (available from the level 1b database) are checked. If certain fatal QC flags are tripped, processing of the target is terminated. A count of the number of QC errors is accumulated by blocks of 500 scan lines to allow bad sections of data to be pinpointed for diagnostic study. The magnitude and consistency of AVHRR and HIRS calibration coefficients are also monitored, and targets with erroneous calibration data are likewise rejected.

Next, one or more processing algorithms are selected: SST (daytime or nighttime), aerosol, etc. (Note that a simultaneous parallel-test mode allows comparison of results from a new algorithm with the result of the operational algorithm, for a selected portion of the global ocean.) The processing algorithm includes identifying targets suitable for the retrievals and performing the retrieval. The specific tests are listed below. For more specifics on their rationale, see McClain et al. (1985), McClain (1989), and Walton et al. (1989).

- 1) *Land-sea test*: The gross land test first checks selected elements from each target against the low-resolution land-sea tag value at the nearest $\frac{1}{2}^\circ$ latitude-longitude intersection: (a) if solar zenith angle $\theta_0 < 26^\circ$, the four target corners are selected; (b) if $26^\circ \leq \theta_0 < 50^\circ$, the four corners and the center are selected; and (c) if $\theta_0 \geq 50^\circ$, the four corners, center, and the two points equidistant from the center and the outside edge on the long axis of the target are selected. If all coordinates selected are over ocean, the target is processed. If all coordinates are over land, the target is not processed. If some coordinates indicate that the target is at a coastal interface, additional checks against high-resolution tags are performed. As a result of this procedure, it is estimated that aerosol retrievals are made no closer than ~ 10 km from the coastline.
- 2) *Gross cloud-glitter visible test*: If albedo in channel 2, $A_2 < 50\%$ for less than 10 GAC pixels (out of a total of $11 \times 11 = 121$), the whole target is rejected. Otherwise, the target is processed.
- 3) *Unit array selection*: A (re)programmable search

table is used to find a 2×2 array within the target in which all four elements have $A_2 < 50\%$.

- 4) *Visible and IR uniformity tests*: In the 2×2 array, if $[\max(C_2) - \min(C_2)] \leq 2$ and $[\max(C_4) - \min(C_4)] \leq 3$, then proceed to test 5. {Here, C_i is the count for channel i , and min/max are determined from the four GAC pixels in the unit array. One channel 2 count is worth $\sim 0.1\%$ albedo [defined later by Eq. (1)], and one channel 4 count is worth $\sim 0.1^\circ\text{C}$ when in cloud-free conditions.}
- 5) *Visible threshold*: If $\max(C_2) < R_{CV}(\theta_0, \theta, \varphi)$, then proceed to test 6. [Here, R_{CV} is the visible cloud threshold table reflectance (for the solar zenith angle, θ_0 ; satellite zenith angle, θ ; and relative azimuth, φ), which is constructed from empirical analysis of observed reflectances collected over a period of normally 3–4 weeks. This table is updated periodically when satellite drift causes R_{CV} to lose its validity due to changing solar/satellite geometry.]
- 6) *Average unit array counts*: The average count for each of five channels for the 2×2 unit array that passes the above tests (2–5) is determined.
- 7) *Calibrating the 2×2 unit array averages*: Using formulas from Goodrum et al. (2003), and calibration coefficients read from level 1b files, the albedos in channels 1, 2, and 3A are calculated as are brightness temperatures in channels 4 and 5, T_4 and T_5 , respectively (see section 4b for calibration detail).
- 8) *Channel 4 threshold test*: If 2×2 average $T_4 < 270$ K, the array is rejected.
- 9) *Channel 4–5 difference test*: If 2×2 average $T_4 - T_5 > 3.5$ K, the array is rejected.
- 10) *Channel 4–5 IR cloud test*: If 2×2 average $T_4 < -11.488987 + 1.0439T_5$, the array is rejected.
- 11) *SST retrieval*: SST is retrieved from T_4 and T_5 using the split-window multichannel (MCSST), and nonlinear, (NLSST) equations (Walton et al. 1998).
- 12) *Reasonable SST test*: If $-2^\circ \leq \text{NLSST} \leq 35^\circ$, then proceed to test 13.
- 13) *SST intercomparison test*: If $|\text{NLSST} - \text{MCSST}| < 1.5^\circ\text{C}$, then proceed to test 14.
- 14) *Computing earth location*: The latitude and longitude of the center of the unit array are determined.
- 15) *Aerosol retrieval*: The value of τ is retrieved from albedos in channels 1, 2, and 3A (see section 4c for detail).
- 16) *Obtaining additional unit arrays*: Additional unit arrays are obtained and tests 4–15 are repeated.
- 17) *Storing aerosol and SST retrievals*: Aerosol and SST retrievals for all unit arrays are stored in the initial storage file.
- 18) *Relaxed tests*: If all unit arrays attempted for any target (up to max number of attempts) failed any test and the relaxed visible cloud test flag is set to “true,” then the “warm spot” subroutine, WRMSPT, is called. The warmest spot in the target closest to its center is used as the corner of four unit arrays, which are run through the uniformity

tests 4 and the relaxed visible cloud test 5. If none of the 2×2 unit arrays pass these tests, the target is finally rejected. If one unit array passes both 4 and 5, it is then tested by the rest of the tests selected for the warm spot mode of operation. Currently, these tests are 8 and 9, and 12 and 13, listed above. If the arrays pass, two additional tests are run while in relaxed mode: *18a) HIRS cloud test*: $D_1 = 3.5 - 0.2333(\text{TH}_8 - \text{TH}_7) + 0.038446 \times \text{SSTFLD} + 1.612(\sec\theta - 1)$, where TH_7 and TH_8 are brightness temperatures in HIRS channels 7 and 8, and SSTFLD is the nearest 100-km analyzed field grid-point SST. Test is failed if $D_1 > D_{10}$, where $D_{10} = 0.5$. *18b) Field test*: $D_2 = |\text{MCSST} - (\text{ASSTFLD}) - (1 - A) \text{SSTCLIM}|$, where SSTCLIM is climatological SST, and $A = 0.666$ is an empirical parameter. Test is failed if $D_2 > D_{20}$, where $D_{20} = 3.0$. Note that *both* 18a and 18b must fail for rejection of the array. (In 18a–18b, the thresholds D_{10} and D_{20} are read in from data files.)

4. Radiometric definitions and aerosol algorithm

This section gives the necessary radiometric and calibration definitions for the AVHRR/3 and provides a brief summary of the aerosol algorithm (for more detail, see Ignatov and Stowe 2002a).

a. Radiometric definitions

The NOAA level 1b solar reflectance channel data used as input for the AEROBS processing provide counts and calibration constants to calculate an overhead sun albedo, A_i , defined physically as

$$A_i(\%) = \frac{100\pi L_i}{F_{0i}}, \quad (1)$$

where i is the reflectance channel (centered at λ_{0i}), L_i ($\text{W m}^{-2} \mu\text{m}^{-1} \text{sr}^{-1}$) is the measured TOA spectral radiance and F_{0i} ($\text{W } \mu\text{m}^{-1} \text{m}^{-2}$) is the spectral TOA solar flux, normalized at a unit sun–earth distance, $d_0 = 1$. However, the albedos defined by Eq. (1) also need to be normalized at $d_0 = 1$, because the TOA radiance, L_i , varies as $1/d^2$. The λ_{0i} and F_{0i} values used in NOAA-KLM processing are listed in Table 1a after Goodrum et al. (2003).

For this study, we have recalculated the values of λ_{0i} and F_{0i} following Ignatov and Stowe (2002a), who compiled the λ_{0i} and F_{0i} data for all pre-KLM satellites. The AVHRR/3 spectral response functions used in the integration have been taken from Goodrum et al. (2003) as shown in Fig. 3 for NOAA-16 and -17. The newly calculated values for λ_{0i} and F_{0i} are listed in Table 1b. Note that the two λ_{0i} results agree well. The F_{0i} differences are within 0.1%–0.3% for AVHRR/3 channels 1 and 2 on NOAA-16 and -17, but reach 1.6%–2.1% in channel 3A, thus signaling a potential source of error.

TABLE 1a. Effective central wavelengths λ_{oi} and “solar constants,” F_{oi} , for three channels of AVHRR/3 on board NOAA-KLM [Goodrum et al. (2003); note that the user’s guide lists values of in-band solar irradiance, F_i (W m^{-2}), and effective width of channel, W_i (μm), from which $F_{oi} = F_i/W_i$]. These parameters are used in the NESDIS operations.

| | Channel 1 ($\lambda_1 = 0.63 \mu\text{m}$) | | Channel 2 ($\lambda_2 = 0.83 \mu\text{m}$) | | Channel 3A ($\lambda_3 = 1.61 \mu\text{m}$) | |
|---------|---|---|---|---|--|---|
| | $\lambda_{o1} (\mu\text{m})$ | $F_{o1} (\text{W m}^{-2} \mu\text{m}^{-1})$ | $\lambda_{o2} (\mu\text{m})$ | $F_{o2} (\text{W m}^{-2} \mu\text{m}^{-1})$ | $\lambda_{o3} (\mu\text{m})$ | $F_{o3} (\text{W m}^{-2} \mu\text{m}^{-1})$ |
| NOAA-15 | 0.632 | 1651.2 | 0.843 | 1032.5 | 1.607 | 240.9 |
| NOAA-16 | 0.632 | 1644.4 | 0.843 | 1034.5 | 1.605 | 243.6 |
| NOAA-17 | 0.634 | 1641.1 | 0.843 | 1031.6 | 1.606 | 242.2 |

According to Eq. (1), the solar flux uncertainties are indistinguishable from the calibration slope errors discussed in section 4b.

The Rayleigh (τ^r) and gaseous (τ^g) optical depths are calculated according to Ignatov and Stowe (2002a) and shown in Tables 2a–c. AVHRR/3 channels 1 and 2 are practically identical to those on AVHRR/2 and hence remain significantly affected by variable ozone and water vapor absorption. Thus, the accuracy of the aerosol retrievals could be improved by specifying the gas concentrations from ancillary sources. Note that for an accurate characterization of the radiative transfer in channel 2, the relative vertical distribution of water vapor and aerosol would need to be specified (not merely the integral water vapor content). The use of total ozone content for correction of channel 1 is more straightforward because ozone is mostly located above the scattering layer. Variations in the Rayleigh optical depth are also a source of error. For instance, a $\pm 5\%$ deviation of the surface pressure from that assumed in the retrievals would result in a $\delta\tau^r \sim \pm 3 \times 10^{-3}$ fluctuation in channel 1, which translates into a $\delta\tau_1 \sim \pm 2 \times 10^{-2}$ AOD error (Ignatov and Nalli 2002). The respective τ^r s in AVHRR/3 channels 2 and 3A are ~ 3 and ~ 50 times smaller compared to channel 1, resulting in a proportionate reduction of the respective τ errors. Using surface pressure in aerosol retrievals would mitigate this source of error. By comparison, the AVHRR/3 channel 3A is relatively clean: both Rayleigh scattering and gaseous absorption are small here, and quite stable.

b. Calibration of AVHRR/3

In operational practice, the AVHRR count in a reflectance channel i , C_i , is directly converted into albedo (bypassing calculation of radiance) using the formula

$$A_i(\%) = S_i C_i + I_i, \quad (2)$$

where S_i is the calibration slope and I_i the intercept. Preflight calibration constants, calculated from the results of laboratory radiance calibration using solar constants in Table 1, are reported in Table 3 after Goodrum et al. (2003). These parameters have been used to calibrate the AVHRR/3 on board all three KLM platforms since their launch.

For NOAA-16, results of the MODIS-based calibration (Heidinger et al. 2002) are also listed in Table 3. The largest difference from preflight numbers is in the channel 3A intercept, I_3 . On 11 February 2003, the troublesome preflight calibration in channel 3A was replaced by the MODIS-based calibration, whereas calibrations in channels 1 and 2 remained preflight. The first NOAA-16 AEROBS dataset with corrected calibration became available shortly thereafter, from 12 to 20 February 2003 (note that it took 8 days for this change to take full effect in the 8-day rotated AEROBS file). Analyses in section 5 will show that the effect of this calibration error on aerosol retrievals was very significant. (Actually, it was our aerosol analyses that first revealed this problem.) Note that this error would be much easier to uncover if the calibration equation were written in a form that uses a zero count, C_{oi} in lieu of the intercept, I_i , as is the operational practice with geostationary satellites (Weinreb et al. 1997):

$$A_i(\%) = S_i(C_i - C_{oi}). \quad (3)$$

Equation (3) emphasizes the use of a “zero count,” which is measured from space view in flight in all reflectance channels in each AVHRR scan line, but which is not used in the current NOAA operations. The use of a measured zero count is particularly beneficial for

TABLE 1b. Same as in Table 1a calculated according to Eqs. (3) and (4) from Ignatov and Stowe (2002a). Percent difference from F_{oi} in Table 1a is also shown in parentheses. Note that these constants are *not* used in NESDIS operations. They are given here for reference only.

| | Channel 1 ($\lambda_1 = 0.63 \mu\text{m}$) | | Channel 2 ($\lambda_2 = 0.83 \mu\text{m}$) | | Channel 3A ($\lambda_3 = 1.61 \mu\text{m}$) | |
|---------|---|---|---|---|--|---|
| | $\lambda_{o1} (\mu\text{m})$ | $F_{o1} (\text{W m}^{-2} \mu\text{m}^{-1})$ | $\lambda_{o2} (\mu\text{m})$ | $F_{o2} (\text{W m}^{-2} \mu\text{m}^{-1})$ | $\lambda_{o3} (\mu\text{m})$ | $F_{o3} (\text{W m}^{-2} \mu\text{m}^{-1})$ |
| NOAA-15 | 0.633 | 1648.1 (−0.2%) | 0.840 | 1039.3 (+0.7%) | 1.607 | 247.0 (+2.5%) |
| NOAA-16 | 0.632 | 1649.3 (+0.3%) | 0.843 | 1032.9 (−0.2%) | 1.605 | 247.6 (+1.6%) |
| NOAA-17 | 0.634 | 1642.4 (+0.1%) | 0.843 | 1032.8 (+0.1%) | 1.606 | 247.2 (+2.1%) |

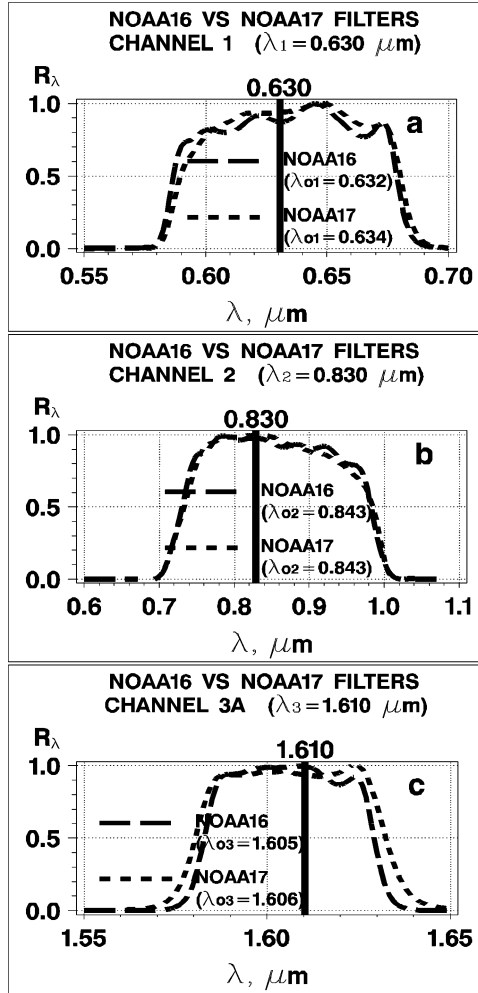


FIG. 3. Spectral response functions, R (dimensionless; normalized to 1 at maximum), in AVHRR/3 channels (a) 1, (b) 2, and (c) 3A on board *NOAA-16* and *-17* satellites. The respective λ_{0i} are superimposed.

aerosol retrievals, given the small signal (low radiance) typically associated with aerosols over ocean. Listed in Table 3 are preflight zero counts determined from I_i and S_i as $C_{0i} = I_i/S_i$. It is immediately clear that the preflight $C_{03} \sim 71.2$ on *NOAA-16* is far off its target value of $C_0 = 40$ (typical C_0 for AVHRR solar reflectance channels is within ± 2 of this target value). As a quick test, the mean and standard space view counts in the three AVHRR/3 channels from one orbit of *NOAA-16* on 1 October 2001 were measured from space view to be $C_{01} \sim 38.9(\pm 0.3)$, $C_{02} \sim 39.3(\pm 0.5)$, and $C_{03} \sim 38.5(\pm 1.3)$. These values clearly differ from the preflight C_{0i} values listed in Table 3, the largest difference occurring in channel 3A. This observation has also been used by Heidinger et al. (2002) to constrain the regression intercepts in AVHRR/3–MODIS intercalibration analyses using actual measurements of zero counts based on space view (cf. their C_{0i} in Table 3). In the next section, the magnitude of the calibration error in channel 3A of the *NOAA-16* AVHRR/3 is independently confirmed with aerosol analyses.

c. Aerosol retrieval algorithm

To avoid specular reflectance from the ocean surface, aerosol retrievals are restricted to the antisolar side of the orbit⁴ outside of the 40° glint cone angle and are reported for solar zenith angles $\theta_0 \leq 70^\circ$ and view zenith angle $\theta \leq 60^\circ$ (the inconsistency between the solar and view zenith angle limits is due to the specifics of the operational cloud mask). AOD in AVHRR/3 channel i ($i = 1, 2, 3A$), τ_i , is estimated from the cloud-free albedo, A_i (normalized at the unit sun–earth distance, $d_0 = 1$) by means of a single-channel lookup table, LUT_i . The satellite and sensor channel-specific LUTs

⁴ The conventional practice probably originated as a means of completely avoiding solar contamination. In an effort to extend the global coverage, analyses are currently under way for the first time to test aerosol retrievals on the solar side of the orbit.

TABLE 2a. Channel 1 ($0.63 \mu\text{m}$) Rayleigh optical depth (Ray1) for different AVHRR/3 (*NOAA-15–17*) sensors and standard atmospheres calculated according to Eq. (5) of Ignatov and Stowe (2002a): TROP, tropical; MLS, midlatitude summer; MLW, midlatitude winter; SS, subarctic summer; SW, subarctic winter; and US62, U.S. standard (1962).

| | τ | TROP | MLS | MLW | SS | SW | US62 |
|----------------|------------------|--------|--------|--------|--------|--------|--------|
| <i>NOAA-15</i> | Ray1 | 0.0565 | 0.0564 | 0.0565 | 0.0561 | 0.0562 | 0.0562 |
| | H ₂ O | 0.0125 | 0.0093 | 0.0030 | 0.0069 | 0.0015 | 0.0048 |
| | O ₃ | 0.0212 | 0.0274 | 0.0341 | 0.0296 | 0.0411 | 0.0295 |
| | O ₂ | 0.0006 | 0.0006 | 0.0006 | 0.0006 | 0.0006 | 0.0006 |
| <i>NOAA-16</i> | Ray1 | 0.0568 | 0.0567 | 0.0568 | 0.0564 | 0.0565 | 0.0566 |
| | H ₂ O | 0.0129 | 0.0096 | 0.0031 | 0.0071 | 0.0016 | 0.0050 |
| | O ₃ | 0.0213 | 0.0274 | 0.0342 | 0.0297 | 0.0412 | 0.0296 |
| | O ₂ | 0.0007 | 0.0007 | 0.0007 | 0.0007 | 0.0007 | 0.0007 |
| <i>NOAA-17</i> | Ray1 | 0.0559 | 0.0558 | 0.0560 | 0.0555 | 0.0556 | 0.0557 |
| | H ₂ O | 0.0115 | 0.0086 | 0.0028 | 0.0064 | 0.0014 | 0.0044 |
| | O ₃ | 0.0209 | 0.0270 | 0.0336 | 0.0292 | 0.0405 | 0.0291 |
| | O ₂ | 0.0010 | 0.0010 | 0.0010 | 0.0010 | 0.0010 | 0.0010 |

TABLE 2b. Same as in Table 2a but for channel 2 (0.83 μm).

| | τ | TROP | MLS | MLW | SS | SW | US62 |
|---------|------------------|--------|--------|--------|--------|--------|--------|
| NOAA-15 | Rayl | 0.0189 | 0.0189 | 0.0190 | 0.0188 | 0.0189 | 0.0189 |
| | H ₂ O | 0.1604 | 0.1361 | 0.0694 | 0.1140 | 0.0441 | 0.0929 |
| | O ₃ | 0.0005 | 0.0006 | 0.0008 | 0.0007 | 0.0010 | 0.0007 |
| | O ₂ | 0.0140 | 0.0140 | 0.0137 | 0.0138 | 0.0134 | 0.0138 |
| NOAA-16 | Rayl | 0.0187 | 0.0187 | 0.0187 | 0.0186 | 0.0186 | 0.0187 |
| | H ₂ O | 0.1661 | 0.1411 | 0.0721 | 0.1182 | 0.0459 | 0.0964 |
| | O ₃ | 0.0005 | 0.0006 | 0.0008 | 0.0007 | 0.0009 | 0.0007 |
| | O ₂ | 0.0138 | 0.0138 | 0.0135 | 0.0136 | 0.0132 | 0.0136 |
| NOAA-17 | Rayl | 0.0187 | 0.0187 | 0.0187 | 0.0186 | 0.0186 | 0.0186 |
| | H ₂ O | 0.1611 | 0.1368 | 0.0699 | 0.1146 | 0.0444 | 0.0934 |
| | O ₃ | 0.0005 | 0.0006 | 0.0007 | 0.0006 | 0.0009 | 0.0006 |
| | O ₂ | 0.0151 | 0.0151 | 0.0148 | 0.0149 | 0.0145 | 0.0149 |

(three channels for each satellite) have been precalculated using the 6S RTM (Vermote et al. 1997) as follows.

The ocean diffuse (Lambertian) component reflectance is set to be globally nonvariable at 0.2%, 0.05%, and 0% in channels 1, 2, and 3A, respectively. These values were determined to represent a net effect of the underlight (for an average chlorophyll concentration) and whitecaps (for an average wind speed) over open ocean. Surface reflectance may be substantially higher over the bright coastal waters and areas with strong winds. Both components are known to decrease with wavelength, making channel 1 the most subject to this type of error. Whitecaps reflectance in channel 2 is $\sim 20\%$ less, and underlight is about 3 times less. Both signals are practically negligible in channel 3A. [See discussion in Ignatov and Stowe (2002a).] Avoiding bright coastal waters, and specifying surface wind and chlorophyll concentration fields elsewhere, would improve the current product. These analyses are currently under way.

A bidirectional (quasi-specular) reflectance component is calculated based upon Cox and Munk (1954) with a fixed wind speed of 1 m s^{-1} . By setting the wind speed that unrealistically low, we avoid the need to specify the wind direction in the Cox–Munk anisotropic formulation used in 6S, although this may underestimate the quasi-specular reflectance signal, especially in the

vicinity of the 40° glint angle (and therefore overestimate the AOD). Including observed wind speed and direction fields within the reflectance calculation would provide a potential for improvements to aerosol retrievals. Note, however, that this may need to be done semi-empirically as evidence emerges that the Cox and Munk (1954) model formulated almost 50 years ago may need revisions and adjustments (e.g., Su et al. 2002 and references therein).

Rayleigh scattering and gaseous absorption are both calculated assuming the midlatitude summer standard atmosphere. Potential improvements are possible by adding global and seasonal distributions of total ozone and water vapor, and surface pressure fields, as has been already discussed in section 4a.

The aerosol size distribution is assumed to be monomodal lognormal, with a mean radius $R_m = 0.10 \mu\text{m}$, $\sigma = 2.03$ (dN/dR), and $n = 1.40 - 0.0i$. Given the data accuracy from the current AVHRR/3, the aerosol model should not be a critical limitation of the current algorithm, as discussed in sections 6 and 7.

Each LUT is calculated taking into account the known spectral response of the channel, and the retrieved τ_i is scaled to the centroid wavelength of the channel, $\lambda_1 = 0.63$, $\lambda_2 = 0.83$, or $\lambda_3 = 1.61 \mu\text{m}$. Note that scaling is done within each channel (see Fig. 3), thus minimizing the interpolation error. Extrapolation beyond the chan-

TABLE 2c. Same as in Table 2a but for channel 3A (1.61 μm).

| | τ | TROP | MLS | MLW | SS | SW | US62 |
|---------|------------------|--------|--------|--------|--------|--------|--------|
| NOAA-15 | Rayl | 0.0013 | 0.0013 | 0.0013 | 0.0013 | 0.0013 | 0.0013 |
| | H ₂ O | 0.0021 | 0.0015 | 0.0004 | 0.0010 | 0.0002 | 0.0007 |
| | CO ₂ | 0.0162 | 0.0162 | 0.0161 | 0.0161 | 0.0159 | 0.0161 |
| | CH ₄ | 0.0007 | 0.0007 | 0.0006 | 0.0006 | 0.0006 | 0.0006 |
| NOAA-16 | Rayl | 0.0013 | 0.0013 | 0.0013 | 0.0013 | 0.0013 | 0.0013 |
| | H ₂ O | 0.0023 | 0.0016 | 0.0005 | 0.0011 | 0.0002 | 0.0008 |
| | CO ₂ | 0.0162 | 0.0162 | 0.0161 | 0.0161 | 0.0159 | 0.0161 |
| | CH ₄ | 0.0005 | 0.0005 | 0.0004 | 0.0005 | 0.0004 | 0.0004 |
| NOAA-17 | Rayl | 0.0013 | 0.0013 | 0.0013 | 0.0013 | 0.0013 | 0.0013 |
| | H ₂ O | 0.0023 | 0.0016 | 0.0004 | 0.0011 | 0.0002 | 0.0007 |
| | CO ₂ | 0.0155 | 0.0155 | 0.0153 | 0.0154 | 0.0151 | 0.0153 |
| | CH ₄ | 0.0009 | 0.0009 | 0.0008 | 0.0009 | 0.0008 | 0.0008 |

TABLE 3. AVHRR/3 preflight low-gain calibration coefficients for NOAA-KLM satellites (Goodrum et al. 2003). Shown in italics are NOAA-16 coefficients derived from intercomparison with Terra-MODIS on 17 May and 5 Jul 2001 (Heidinger et al. 2002).

| | Channel 1 ($\lambda_1 = 0.63 \mu\text{m}$) | | | Channel 2 ($\lambda_2 = 0.83 \mu\text{m}$) | | | Channel 3A ($\lambda_3 = 1.61 \mu\text{m}$) | | |
|--------------------------|---|--------------|--------------|---|--------------|--------------|--|---------------|--------------|
| | S_1 | I_1 | C_{01} | S_2 | I_2 | C_{02} | S_3 | I_3 | C_{03} |
| NOAA-15 (preflight) | 0.0568 | -2.1874 | 38.51 | 0.0596 | -2.4096 | 40.43 | 0.0275 | -1.0684 | 38.85 |
| NOAA-16 (preflight) | 0.0523 | -2.016 | 38.55 | 0.0513 | -1.943 | 37.88 | 0.0287* | -2.043* | 71.18 |
| NOAA-16 (MODIS based) | <i>0.0539</i> | <i>-2.12</i> | <i>39.33</i> | <i>0.0603</i> | <i>-2.35</i> | <i>38.97</i> | <i>0.0262*</i> | <i>-1.01*</i> | <i>38.55</i> |
| NOAA-17 (preflight) | 0.0555 | -2.2193 | 39.99 | 0.0543 | -2.1227 | 39.09 | 0.0265 | -1.1153 | 42.09 |

* On NOAA-16, channel 3A calibration was changed from preflight to MODIS based on 11 Feb 2003.

nels' spectral ranges is avoided (Ignatov and Stowe 2002a). Using a standard set of centroid wavelengths makes retrievals from different NOAA platforms (in particular, from NOAA-16 and -17) directly comparable.

From AODs retrieved in either pair of channels, i and j , τ_i and τ_j , an effective Ångström exponent (AE) is given by

$$\alpha_{ij} = \Lambda_{ij} \ln\left(\frac{\tau_i}{\tau_j}\right), \quad \Lambda_{ij} \equiv -\frac{1}{\ln\left(\frac{\lambda_i}{\lambda_j}\right)}. \quad (2)$$

For AVHRR/3 channels 1, 2, and 3A, the respective spectral amplification factors are $\Lambda_{12} \approx 3.627$, $\Lambda_{13} \approx 1.066$, and $\Lambda_{23} \approx 1.509$. Note that for the fixed monomodal aerosol microphysical model used in the retrievals, the values of the AEs are also fixed at $(\alpha_{12})_0 \approx 0.94$, $(\alpha_{13})_0 \approx 1.25$, and $(\alpha_{23})_0 \approx 1.38$, respectively. However, the AE estimated with Eq. (4), α_{ij} , tends to be closer to the intrinsic AE of the real aerosol rather than to the model $(\alpha_{ij})_0$. This is because the AODs derived with a prescribed aerosol microphysics are subject to *multiplicative* errors, *coherent* in the channels, which largely cancel out when taking the τ ratio into account while calculating the AE (Ignatov and Stowe 2000, 2002a). This cancellation works better for a spectrally closer pair of channels 1 and 2, whose phase functions are very similar, though worse when channel 3A is involved. For the operational AEROBS retrievals, the resulting residual error in α is deemed to be tolerable (Ignatov and Stowe 2000, 2002a).

5. Analyses of τ retrievals

In this section, we present examples of the AOD products from NOAA-16 and -17 during the first 8-day period (12–20 February 2003) after the calibration in channel 3A of NOAA-16 AVHRR/3 was adjusted. The products are preliminarily tested with the *global* self-consistency checks proposed elsewhere (Ignatov and Stowe 2000, 2002b; Ignatov and Nalli 2002), and with the newly

introduced interconsistency (cross-platform) checks.⁵ Note that the former studies suggest that $\sim 1\%$ of τ data are bad (outliers), and τ retrievals at low sun angle ($\theta_0 > 60^\circ$) are biased low. Ideally, both should have been removed before the self- and interconsistency analyses. However, such preprocessing was beyond the scope of the present paper and not attempted here. Comprehensive QC of the KLM aerosols is currently under way and results will be presented elsewhere.

a. Global maps

Figure 4 shows global 8-day average distributions of AOD derived from NOAA-16 and -17. The pixel-level τ retrievals have been mapped into $(1^\circ)^2$ grids and averaged over the 8-day period, forming $N = 29\,748$ and $N = 29\,177$ [$8 \text{ day} \times (1^\circ)^2$] boxes for NOAA-16 and -17, respectively. Data populated in $N = 26\,083$ of these boxes are common to both satellites, thus indicating that the aerosol spatial coverage and cloud cover are similar from the midmorning and afternoon platforms.

The spatial and spectral τ patterns are largely self-consistent from both NOAA-16 and -17, and interconsistent between the two platforms. Although the observed features are in a broad qualitative agreement with the available knowledge on the aerosol distribution over the global ocean (e.g., Husar et al. 1997; Wagener et al. 1997; King et al. 1999; Myhre et al. 2004), some inconsistencies are clearly traced within each individual product and between the two satellites. In particular, the NOAA-17 τ_1 is elevated with respect to its NOAA-16 counterpart, whereas τ_2 and τ_3 are somewhat the opposite. These features are thought to be chiefly due to the AVHRR calibration uncertainties. Analyses below provide a more quantitative perspective to these qualitative observations.

⁵ Note that while passing the *global* checks is a necessary condition for the product quality assurance, it may be not sufficient. Looking at the entire globe as one dataset may mask possible problems, which could be better revealed by examining regions and events. These analyses will be conducted once the major issues with the data and algorithm uncovered by the global checks are fixed.

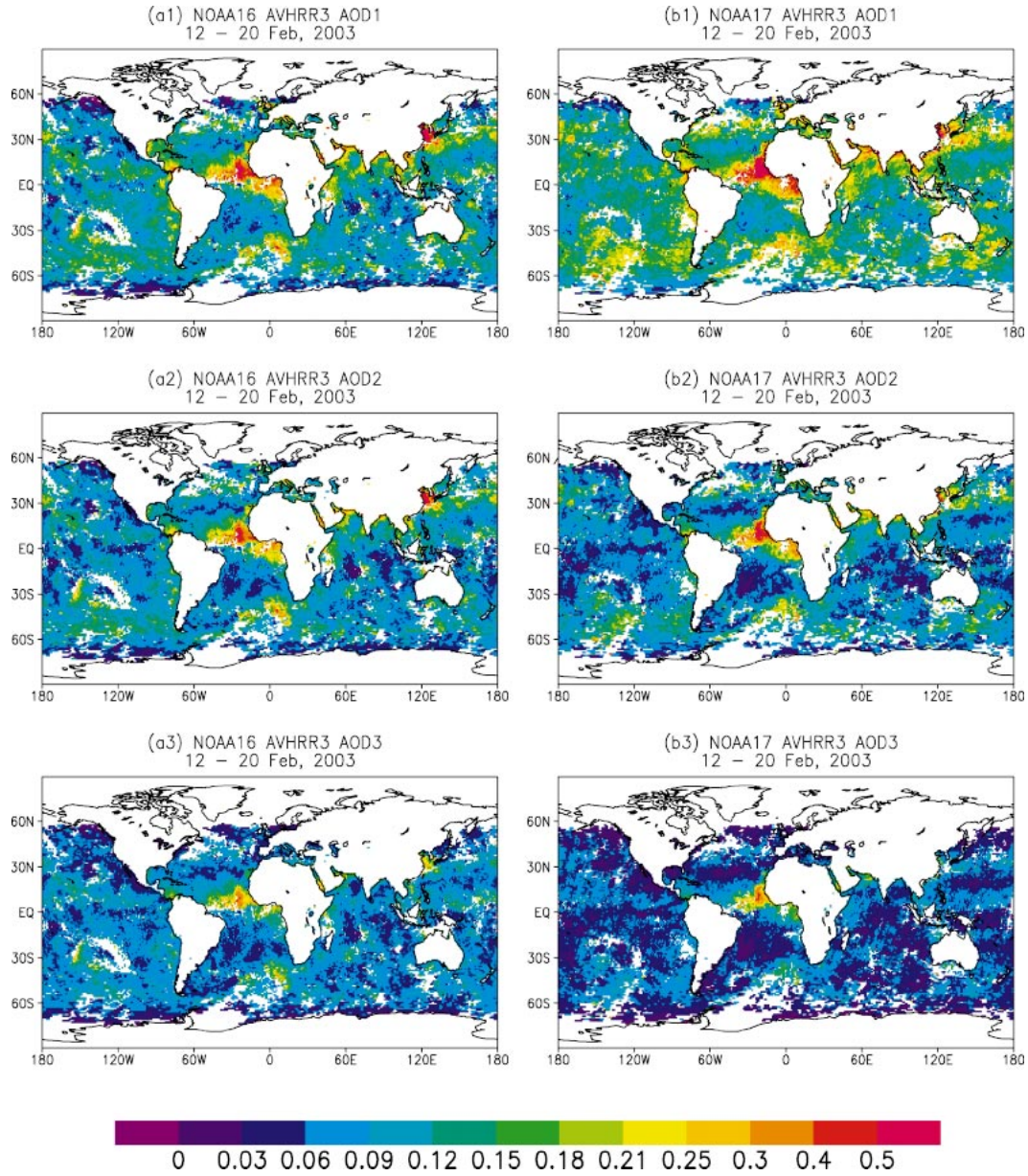


FIG. 4. Global distribution of AOD over oceans derived from AVHRR/3 channels 1) 1 ($\lambda_1 = 0.63 \mu\text{m}$), 2) 2 ($\lambda_2 = 0.83 \mu\text{m}$), and 3) 3A ($\lambda_3 = 1.61 \mu\text{m}$) on board (a) *NOAA-16* and (b) *NOAA-17*. Note that each point on the map is an $[8 \text{ day} \times (1^\circ)^2]$ average.

b. Histograms of τ

Figure 5 plots global τ histograms, from the respective panels of Fig. 4 (note that pixel-level daily τ data were used to plot Fig. 5). The shape of all histograms is close to lognormal as expected (cf. O'Neill et al. 2000; Ignatov and Stowe 2002b; Ignatov and Nalli 2002). For each distribution, the geometric mean, τ_g , and standard deviation, μ , have been calculated in channel i as

$$\log \tau_{gi} = \langle \log \tau_i \rangle; \quad \log \mu_i = \sqrt{\langle (\log \tau_i - \log \tau_{gi})^2 \rangle}. \quad (5)$$

(Note that throughout this paper, shorthand notations, “log” and “ln,” refer to decimal, \log_{10} , and natural, \log_e , logarithms, respectively.) The computed τ_g and μ values are given in the respective panels of Fig. 5. In channels 1 and 2, the estimated τ_g s tend to be biased low with respect to their expected values of $\tau_g \sim 0.12$ and $\tau_g \sim 0.11$ (e.g., Ignatov and Nalli 2002). Prior observations of τ_3 (at $1.61 \mu\text{m}$) are scarce, making evaluation of the retrievals from this channel less straightforward. The intersatellite differences are statistically significant in all three channels. Since the τ_g and μ

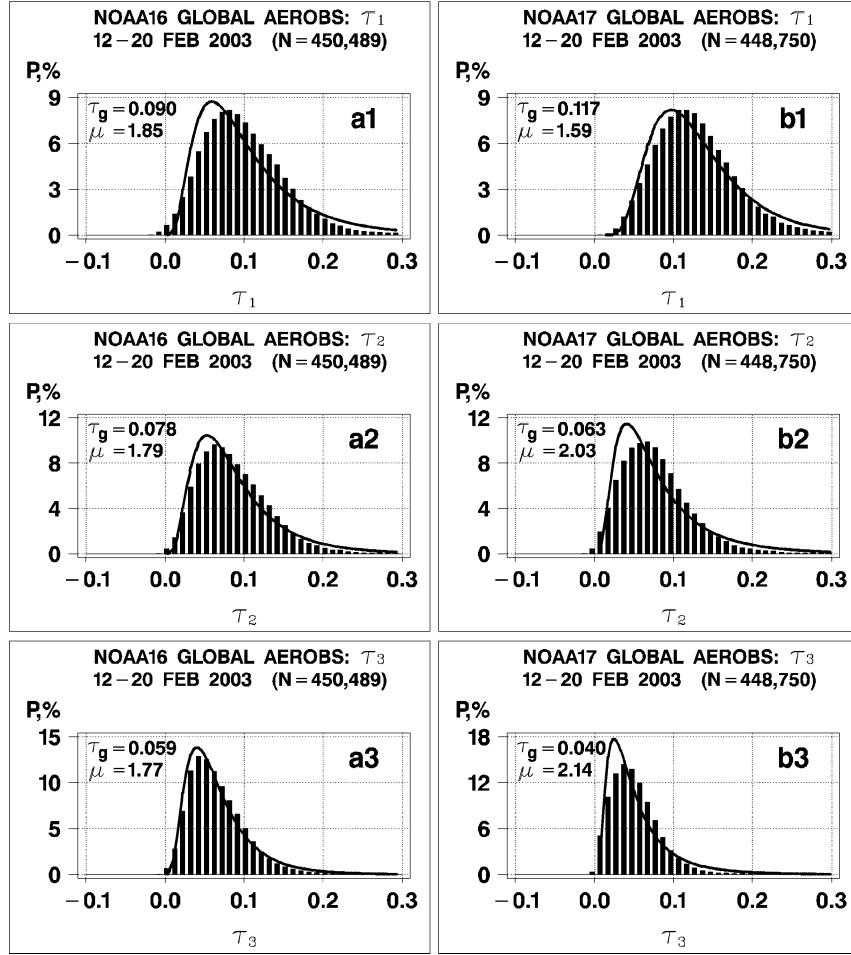


FIG. 5. Empirical histograms (needles centered on $\Delta\tau = 10^{-2}$ bins), and their fit with lognormal probability distribution functions (PDFs) (solid line), of 1) τ_1 , 2) τ_2 , and 3) τ_3 from (a) NOAA-16 and (b) NOAA-17. Note that the original GAC-level daily data were used in plotting these histograms.

parameters are subject to data errors from outliers and biases, their more in-depth quantitative analyses are deemed to be premature at this time and were not attempted here.

The respective lognormal fits are also superimposed in the panels of Fig. 5:

$$P(\tau_i) = \frac{P(\log \tau_i)}{\tau_i \ln 10};$$

$$P(\log \tau_i) = \frac{1}{\sqrt{2\pi} \log(\mu_i)} \exp \left[-\frac{\log^2 \left(\frac{\tau_i}{\mu_i} \right)}{2 \log^2(\mu_i)} \right]. \quad (6)$$

The empirical τ histograms may deviate from their lognormal fits due to the nonuniformity of the global aerosol sample. However, the wide diversity of the patterns of deviations in different channels is thought to result mainly from data errors. The closest agreement between

the data and fit happens to occur in channel 3A of NOAA-16 (Fig. 4a3), which is the only one (out of six) calibrated postlaunch.⁶

The inter- and intrasatellite changes in the values of the τ_g parameters, and in the shape of the τ histograms in Fig. 5, do not reveal any systematic pattern. This suggests that the AVHRR/3 calibration uncertainty is the most plausible cause, not aerosol physics. Uncertainties in the calibration slope and intercept (or zero count) may contribute to aerosol errors as follows.

- 1) *Calibration slope.* S_i : Respective errors in AVHRR/2 channels 1 and 2 are well approximated as $\Delta\tau_1 \sim (0.37 + 0.71\tau_1)\varepsilon_1$ and $\Delta\tau_2 \sim (0.16 + 0.74\tau_2)\varepsilon_2$, where $\varepsilon_i = \Delta S_i/S_i$ is the fractional calibration slope error (Ignatov 2002). No empirical estimates are available for channel 3A, but simple theoretical con-

⁶ Note that the MODIS-based calibration used here was obtained in May–June 2001, almost 2 yr before February 2003.

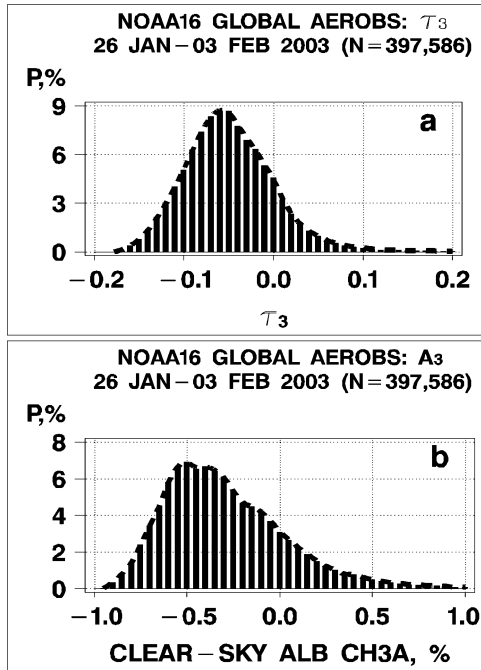


FIG. 6. Histograms (bars centered on $\Delta\tau = 10^{-2}$ bins) of (a) τ_3 and (b) A_3 from NOAA-16 AVHRR/3, before calibration in AVHRR/3 channel 3A was adjusted on 11 Feb 2003 from preflight (Goodrum et al. 2003) to MODIS based (Heidinger et al. 2002).

siderations [Eq. (13) in Ignatov (2002)] suggest that, to a first approximation, $\Delta\tau_3 \sim (0.0 + 1.0\tau_3)\epsilon_3$. An error in the calibration slope thus leads to a linear transformation of the aerosol field as a whole without changing its spatial patterns. The similarity between the AOD spatial distributions from NOAA-16 and -17 for all three channel pairs in Fig. 4 may suggest that the calibration differences are the major causes of the absolute differences in AOD.

- 2) *Calibration intercept, I_i (or zero count, C_{0i}):* A significant τ error may result from an incorrect C_{0i} (which we recall is measured on board, but not used in the current NOAA operations). Figure 6a shows a histogram of τ_3 , derived from AVHRR/3 channel 3A on NOAA-16 before its calibration was adjusted on 11 February 2003. Figure 6b further shows a histogram of the clear-sky albedo in this channel used to retrieve τ_3 in Fig. 6a. More than 90% of both A_3 data, and τ_3 derived therefrom, are negative. Table 3 shows that the major problem with the preflight calibration was the intercept not the slope. Note that Eq. (15) in Ignatov (2002) suggests that an error in zero count affects τ retrievals differently at different view angles, thus causing spatial distortions to the AOD fields.

c. Scattergrams of τ_i versus τ_j from the same platform

The AODs are expected to change coherently with wavelength. Figure 7 shows scattergrams of retrieved

τ_i versus τ_j from NOAA-16 and -17. The retrievals are expected to fill in a two-dimensional sector, restricted by two straight lines corresponding to approximately $\alpha = 0$ [$\tau_i = \xi_{ij}^{(0)}\tau_j$, where $\xi_{ij}^{(0)} = 1.0$] and $\alpha = 2$ ($\tau_i \approx \xi_{ij}^{(2)}\tau_j$; where $\xi_{12}^{(2)} \approx 1.736$; $\xi_{13}^{(2)} \approx 6.531$, and $\xi_{23}^{(2)} \approx 3.763$) and shown with long dashes.⁷ Here, the $\xi_{ij}^{(0)}$ and $\xi_{ij}^{(2)}$ are the slopes of the boundary lines, which have been calculated from the respective AEs using Eq. (4). The least squares regression lines through the data are also superimposed with short dashes, and the respective equations are given in the lower right-hand corners.

It can be seen that the actual data are displaced from their expected domains. The displacement is different for different pairs of channels. The largest displacements are found in the NOAA-17 pairs that use channel 1 data. In all cases, some points fall outside of the main cluster. Their physical nature is well understood and procedures to identify and remove those points have been proposed (Ignatov and Stowe 2002b). In particular, the proportion of high outliers is larger when channel 1 is involved and smaller for the pair of channels 2 and 3A. These data points occur over bright turbid waters where reflectance quickly decreases with wavelength. These points can be removed by QC analyses in future work.

Another observation that clearly emerges from Fig. 7 is a comparative potential of the three pairs of channels for estimation of the Ångström exponent. The sector between the two lines corresponding to $\alpha = 0$ and $\alpha = 2$ is narrowest for channels 1 and 2, and widest for channels 1 and 3A, suggesting that the latter pair is much less sensitive to measurement errors in individual channels, whereas the 2–3A pair is found somewhere between these two. Note that the width of the sector indicates the α sensitivity to τ errors, whereas the actual α error also depends upon the magnitude of those errors in individual channels. In particular, the τ error is expected to be smallest in channel 3A followed by channel 2 (which is, however, contaminated by strong water vapor absorption). It is yet to be determined empirically how these two factors counterbalance each other in the resulting AE for different pairs of channels.

d. Cloud–aerosol correlations

Visual inspection of Fig. 4 suggests that the retrieved AODs tend to be elevated around the “white spots” where cloud have been persistent during the 8-day period. Cloud amount information is not available from the AEROBS files. We thus use the number of clear 8-km AEROBS pixels within $[1 \text{ day} \times (1^\circ)^2]$ boxes, N_A , as a surrogate for the (inverse) cloud amount. Analyses in Ignatov and Nalli (2002; see their Fig. 14) suggest that the cloud amount and N_A are highly intercorrelated.

⁷ The AE is known to depend on the spectral interval (see, e.g., different values of α_{ij} for the fixed aerosol model used in this study; section 4c). However, the same range from 0 to 2 was adopted here for all three AEs, for the sake of illustration.

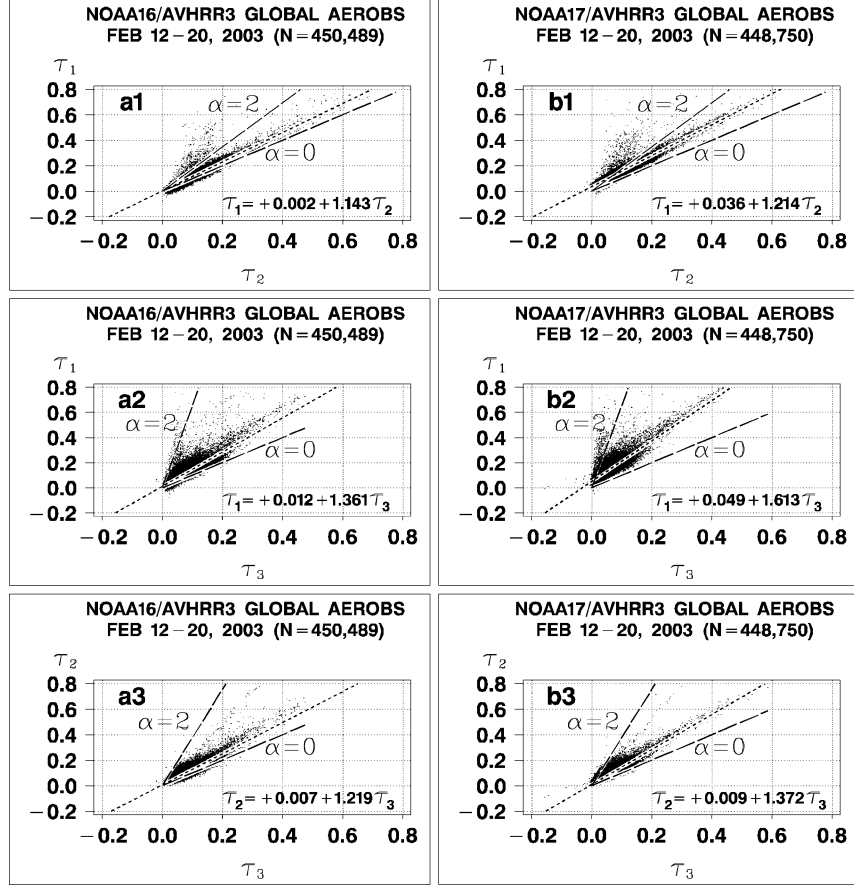


FIG. 7. Scattergrams of 1) τ_1 vs τ_2 , 2) τ_1 vs τ_3 , and 3) τ_2 vs τ_3 derived from (a) NOAA-16 and (b) NOAA-17. Short dashes show regression lines, with regression equations $\tau_1 = b + a\tau$, superimposed. Long dashes correspond to $\alpha = 0$ and $\alpha = 2$.

In our data samples, there are a total of $N = 66\,873$ and $N = 63\,491$ [$1 \text{ day} \times (1^\circ)^2$] boxes with at least one aerosol observation ($N_A \geq 1$) for NOAA-16 and -17, respectively. Frequency distributions of N_A in Fig. 8 (top panels) are similar from the two platforms, and they do not indicate any statistically significant differences in cloud cover between the morning and afternoon. The $\tau(N_A)$ trends are clearly traced in all channels of both satellites when $N_A \leq 8$, and they flatten out at $N_A > 8$. The amplitudes of the effect (defined here as $\delta\tau_i = \tau_i(N_A = 1) - \tau_i(N_A = 8)$) are $\delta\tau_1 \sim 0.05$, $\delta\tau_2 \sim 0.04$, and $\delta\tau_3 \sim 0.03$ in channels 1, 2, and 3A, respectively. Note that there are only $N = 11\,724$ (NOAA-16) and $N = 12\,534$ (NOAA-17) [$1 \text{ day} \times (1^\circ)^2$] boxes with $N_A > 8$. This is only $\sim 20\%$ of the data, suggesting that AODs in all three channels are biased high with respect to the “100% clear sky” case in every four out of five [$1 \text{ day} \times (1^\circ)^2$] boxes. The nature of this bias is not immediately clear. Plausible explanations include data problems (residual cloud in the AEROS pixels, stray light, and adjacency effects) or physical cloud–aerosol interaction. More analyses are needed to better understand and resolve the physical mechanisms underlying these trends.

e. Cross-platform comparisons

Ground-based analyses by Kaufman et al. (2000) suggest that the retrievals at 1000–1030 and 1330–1400 are comparable in magnitude to one another, and to the daily mean. Merging the [$1 \text{ day} \times (1^\circ)^2$] boxes from the two platforms yields a total of $N = 20\,030$ boxes globally in the 8-day period. Figure 9 shows the cross-satellite τ scattergrams. In all three channels, the correlation coefficient, R (given in the upper-left corners), is better than 0.74. This is deemed to be a good result, especially considering that the data have not been subjected to quality control. Subsequent removal of outliers and biased retrievals at high sun, as well as accounting for the calibration problems, will improve the cross-platform correlations.

The monotonic decrease of correlation with wavelength is thought to portray the respective signal-to-noise ratios in the three AODs. Although the τ errors are largest in channel 1, and smallest in channel 3A, the relative strengths of the τ signals are also greatest in channel 1 and smallest in channel 3A. It appears that the spectral decrease in the τ signal may occur at a faster

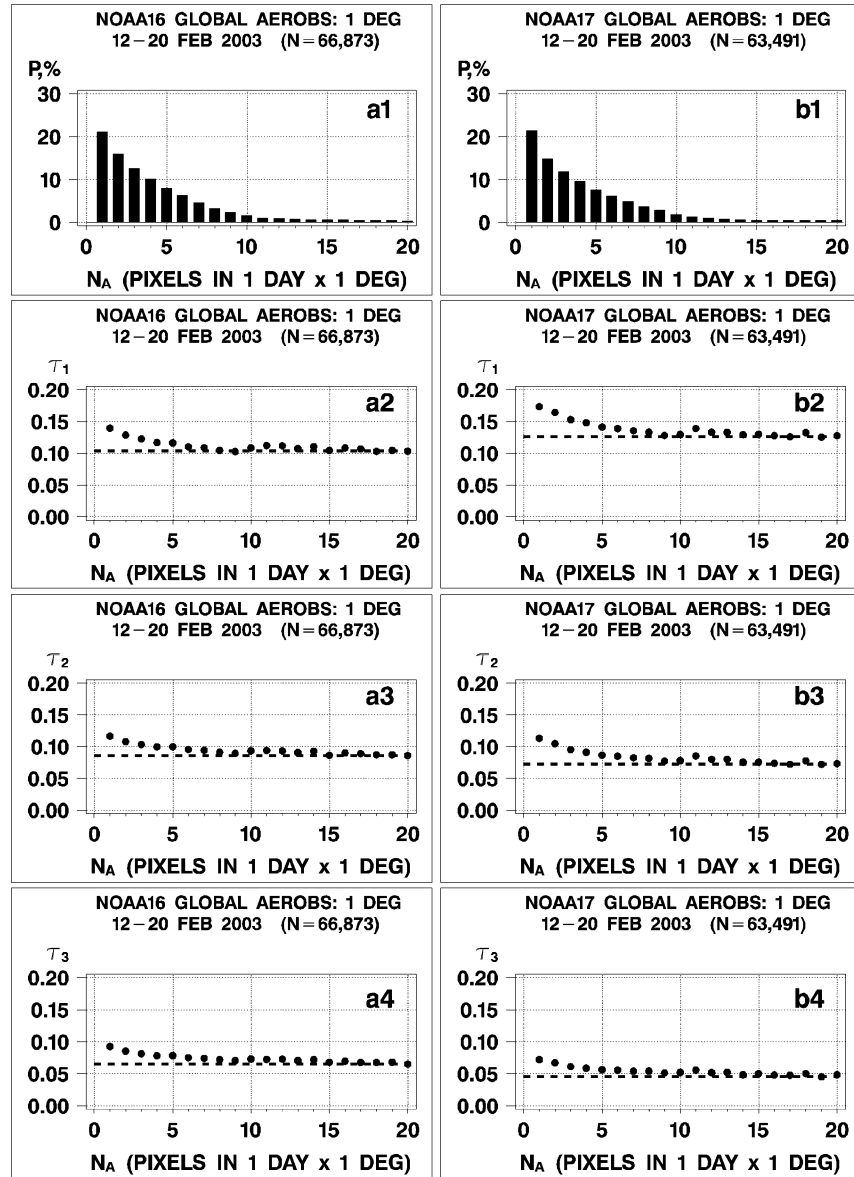


FIG. 8. 1) Histograms of the number of aerosol pixels within $[1 \text{ day} \times (1^\circ)^2]$ boxes, N_A (centered at $\Delta N_A = 1$), and average trends in 2) τ_1 , 3) τ_2 , and 4) τ_3 from (a) NOAA-16 and (b) NOAA-17. Horizontal dashed lines are at the respective $\tau_i(N_A = 20)$.

pace than the respective decrease in τ errors. More analyses are needed to verify this preliminary observation.

The coefficients of the regression are purposely withheld, because they would be inappropriate, and even misleading, in this particular case. Standard least squares regression will effectively minimize errors in the *dependent* variable, y , but only assuming that the *independent* variable, x , is more accurate. The correlation coefficient, on the other hand, is insensitive to the choice of *dependent* and *independent* variables. In our case when both x and y are equally (in)accurate, using the τ differences, $\Delta \tau_i = \tau_{i,17} - \tau_{i,16}$, may be more

appropriate. Figure 10 plots histograms of $\Delta \tau_i$, with their mean and rms statistics superimposed. The biases of $\Delta \tau_1 \sim +3.1 \times 10^{-2}$, $\Delta \tau_2 \sim -0.7 \times 10^{-2}$, and $\Delta \tau_3 \sim -1.9 \times 10^{-2}$ chiefly result from the calibration differences in the three respective pairs of channels. The rms differences of $\sigma \tau_1 \sim 0.05$, $\sigma \tau_2 \sim 0.04$, and $\sigma \tau_3 \sim 0.03$ result from a number of factors, such as the spatial and temporal variability in the τ fields [recall that the $\tau_{i,17}$ and $\tau_{i,16}$ data may come from different corners of a $(1^\circ)^2$ box and are separated in time by an average of ~ 4 h], differences in instantaneous cloud cover during NOAA-16 and -17 overpasses, and radiometric noise and

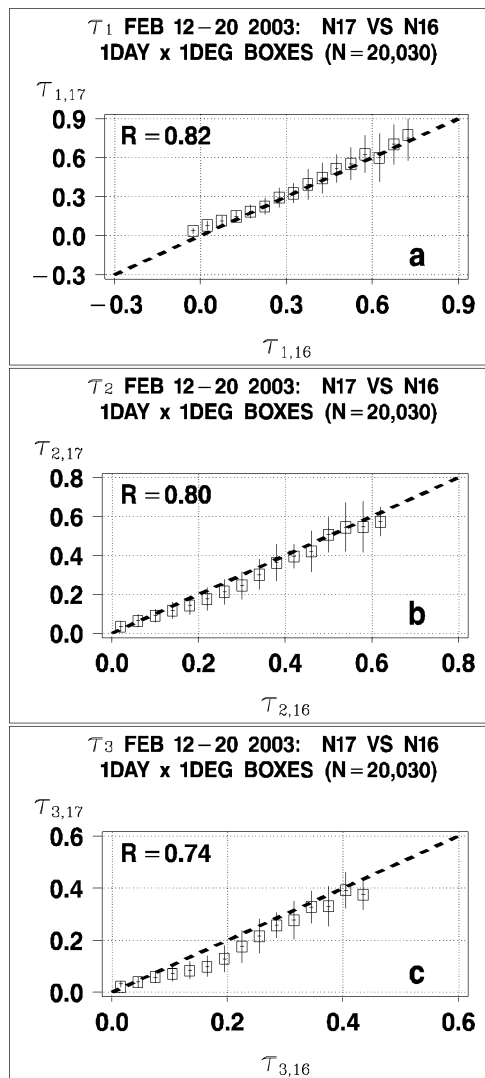


FIG. 9. Scattergrams of NOAA-17 vs NOAA-16 AODs (a) $\tau_{1,17}$ vs $\tau_{1,16}$, (b) $\tau_{2,17}$ vs $\tau_{2,16}$, and (c) $\tau_{3,17}$ vs $\tau_{3,16}$. Data are binned in $\Delta\tau_{1,16} = 0.05$, $\Delta\tau_{2,16} = 0.04$, and $\Delta\tau_{3,16} = 0.03$ intervals, and mean/std. dev. statistics of the respective τ_{17} s are plotted. Respective correlation coefficients (calculated before binning) are superimposed.

digitization in the AEROS product. Aerosol algorithm errors (e.g., due to variations in surface reflectance in space and time, and different domains of scattering and reflection angles from the midmorning and afternoon platforms), also contribute to the differences. It is the subject of future work to quantitatively attribute these causes.

6. Analyses of α retrievals

The empirical analyses in the previous section illustrate the well-known fact that the accurate retrieval of the aerosol amount from space is a difficult task, even over oceans. Estimating the Ångström exponent, related to the particle fine structure (size) presents an even

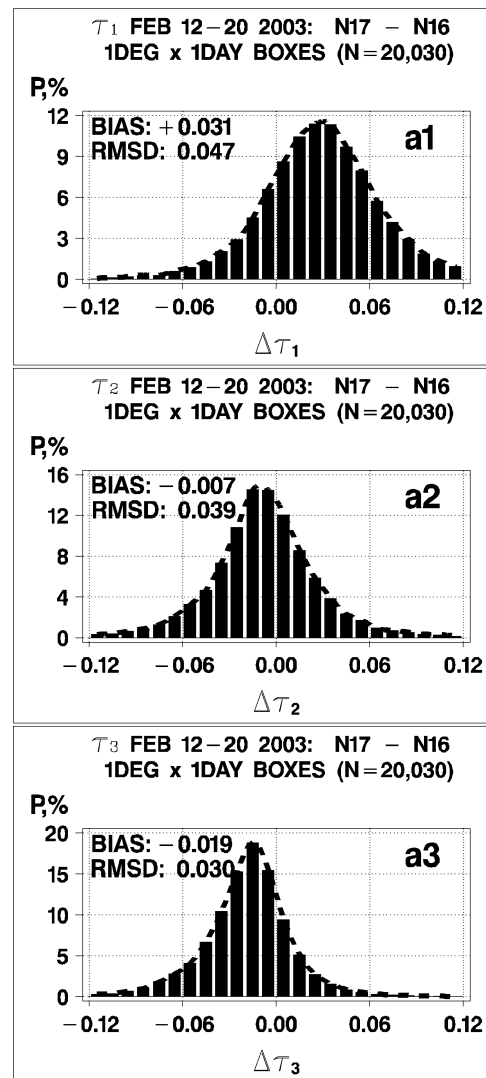


FIG. 10. Histograms (bars centered on $\Delta\tau = 10^{-2}$ bins) of differences between NOAA-17 and NOAA-16 retrievals: (a1) $\Delta\tau_1 = \tau_{1,17} - \tau_{1,16}$, (a2) $\Delta\tau_2 = \tau_{2,17} - \tau_{2,16}$, and (a3) $\Delta\tau_3 = \tau_{3,17} - \tau_{3,16}$. Note that [1 day \times (1°)²] data were used to calculate the differences.

greater challenge because the physical α signal is strongly smeared by noise.

a. Signal and noise in α

The background information below is essential for understanding the empirical results of this section. More detail is found in Ignatov et al. (1998), Ignatov (2002), Ignatov and Stowe (2002b), and Ignatov and Nalli (2002).

The error-free AE is distributed normally, with a standard deviation (STD) of $\sigma_{\alpha 0} \sim 0.3$ (the a priori uncertainty, or the “ α signal”). The bulk of maritime sun photometer measurements report α in the range from approximately 0 to 2, with a modal α value from 0 to 1 (e.g., Smirnov et al. 2002). Apart from the natural

variability, the AE retrieved from space is subject to a number of data- and algorithm-related errors. In the current AVHRR formulation, *multiplicative* τ errors (resulting from using a fixed aerosol model in the retrievals) are *coherent* in the channels and thus largely cancel out when taking the τ ratio in Eq. (4). However, the *additive* errors (e.g., resulting from calibration errors or deviations of the ocean reflectance from that assumed in the retrieval model) do not cancel out. Moreover, the respective α errors get amplified in inverse proportion to τ :

$$\delta\alpha_{ij} = \Lambda_{ij} \left(\frac{\delta\tau_i}{\tau_i} - \frac{\delta\tau_j}{\tau_j} \right) \equiv \frac{\alpha_e}{\tau_k}. \quad (7)$$

[Note that the “ τ_k ” in Eq. (7) is specified at an arbitrary reference wavelength, λ_k , which may not necessarily be either one of λ_i or λ_j .] The retrieval point specific values of α_e result from the τ errors in the two channels, $\delta\tau_i$ and $\delta\tau_j$, which are added together with their signs, and then scaled by the respective spectral amplification factor, Λ_{ij} . A scattergram of “ α versus τ ” for an ensemble of data (e.g., the 8-day global AEROS) may thus reveal two major features. 1) A $1/\tau$ -type average trend, $\langle\alpha_e\rangle/\tau_k$, when ensemble average α_e , $\langle\alpha_e\rangle \neq 0$. If observed, this feature is indicative of systematic error(s) in τ . (Note that the trend analysis does not suggest a specific way to mitigate the systematic τ errors, but it is useful to identify their presence.) 2) A $1/\tau$ -type noise around the trend with STD of $\alpha_{en} \sim \alpha_{ae}/\tau_k$, where σ_{ae} is the ensemble STD of α_e . If observed, this feature is indicative of random errors in τ (which can be reduced by averaging). A signal-to-noise ratio (SNR) is defined as $\eta \sim \sigma_{\alpha 0}/\sigma_{en} \equiv (\sigma_{\alpha 0}/\sigma_{ae})\tau_k \equiv \tau_k/\tau_{k0}$, where $\tau_{k0} \equiv \sigma_{ae}/\sigma_{\alpha 0}$ is a threshold τ_k , at which noise in the retrieved α compares to the signal. For AVHRR/2 channels 1 and 2 (α_{12}), τ_{10} (at $0.63 \mu\text{m}$) ~ 0.18 in the 8-km resolution AEROS data (Ignatov and Stowe 2002b). [For comparison, $\tau_{10} \sim 0.11$ in the 110-km resolution PATMOS data; Ignatov and Nalli (2002).] The τ histograms in Fig. 5 show that there is little data with $\tau_1 \gg \tau_{10}$. Thus in the vast majority of AEROS retrievals, the errors in α_{12} exceed their natural variability. The low SNR in α_{12} is mostly due to the spectral proximity of AVHRR channels 1 and 2 (the spectral amplification factor, $\Lambda_{12} \approx 3.627$). If the τ errors in channel 3A were comparable to those in channels 1 and 2 (which is not exactly true as discussed in section 5c), then the noise in the α_{13} and α_{23} would be reduced by a factor of $\Lambda_{12}/\Lambda_{13} \sim 3.4$ and $\Lambda_{12}/\Lambda_{23} \sim 2.4$, respectively. The analyses of α_{ij} retrievals from NOAA-16 and -17 below in this section will be shown to be in broad qualitative agreement with these simple estimates.

b. Global maps

Figure 11 shows the global ocean distribution of the three AEs derived from different pairs of AVHRR/3

channels on NOAA-16 and -17. From the same platform, the three α fields are expected to correlate well, with the exception of two features that result from deviations of the aerosol size distribution from Junge’s power law: 1) systematic differences in AEs derived from different pairs of channels [e.g., recall that $(\alpha_{12})_0 \approx 0.94$, $(\alpha_{13})_0 \approx 1.25$, and $(\alpha_{23})_0 \approx 1.38$ for the fixed lognormal aerosol microphysics used in the retrievals] and 2) random differences, due to variation in aerosol microphysics from one retrieval point to the other.

NOAA-16: The three AEs from NOAA-16 are within their expected range from 0 to 2, and generally agree well. The α_{12} shows more spatial variability and noise than its two counterparts, α_{13} and α_{23} . Elevated α_{12} occurs in the tropical areas whereas low biases occur in the polar regions (in both an absolute sense and relative to the average), with more variability around the “white spots” with persistent cloud. The spatial patterns in α_{13} and α_{23} are less noisy. In particular, they show more clearly an elevated AE around the coast of southeastern Asia. Aerosol particles are expected to be smaller in the coastal areas, as they are strongly influenced by continental sources. On the other hand, the surface reflectance may also be somewhat elevated near the coast. Both coastal aerosol and bright coastal waters have a sharp spectral dependence; thus, both could feasibly be contributing to elevated AE similar to that observed in Figs. 11a2–a3. (Note that the α_{23} should be least affected by this effect.) More analyses are needed to clearly distinguish between the surface and aerosol signals in the satellite τ and AE retrievals. Interestingly, the AE of the Saharan dust off the west coast of Africa shows only a modest difference from that of the ambient background aerosol.

NOAA-17: All three AEs from NOAA-17 are biased high with respect to NOAA-16. The largest bias is observed in α_{12} , which is also significantly displaced from its expected range from 0 to 2. The bias is smaller in α_{13} , and further decreases in α_{23} where it mostly concentrates in high latitudes. These features in retrieved AE are deemed to result from AVHRR/3 calibration errors (which we recall is prelaunch in all channels except 3A on NOAA-16).

Any geophysical evaluation of the α spatial patterns is thus deemed to be premature from NOAA-16, and especially NOAA-17, until these data errors are corrected.

c. Histograms of the Ångström exponent

Figure 12 shows empirical histograms of the AEs, along with their normal fit given by

$$P(\alpha) = \frac{1}{\sqrt{2\pi}\sigma_\alpha} \exp\left[-\frac{(\alpha - \alpha_m)^2}{2\sigma_\alpha^2}\right]. \quad (8)$$

The ensemble arithmetic mean, α_m , and STD, σ_α , are also provided in Fig. 12.

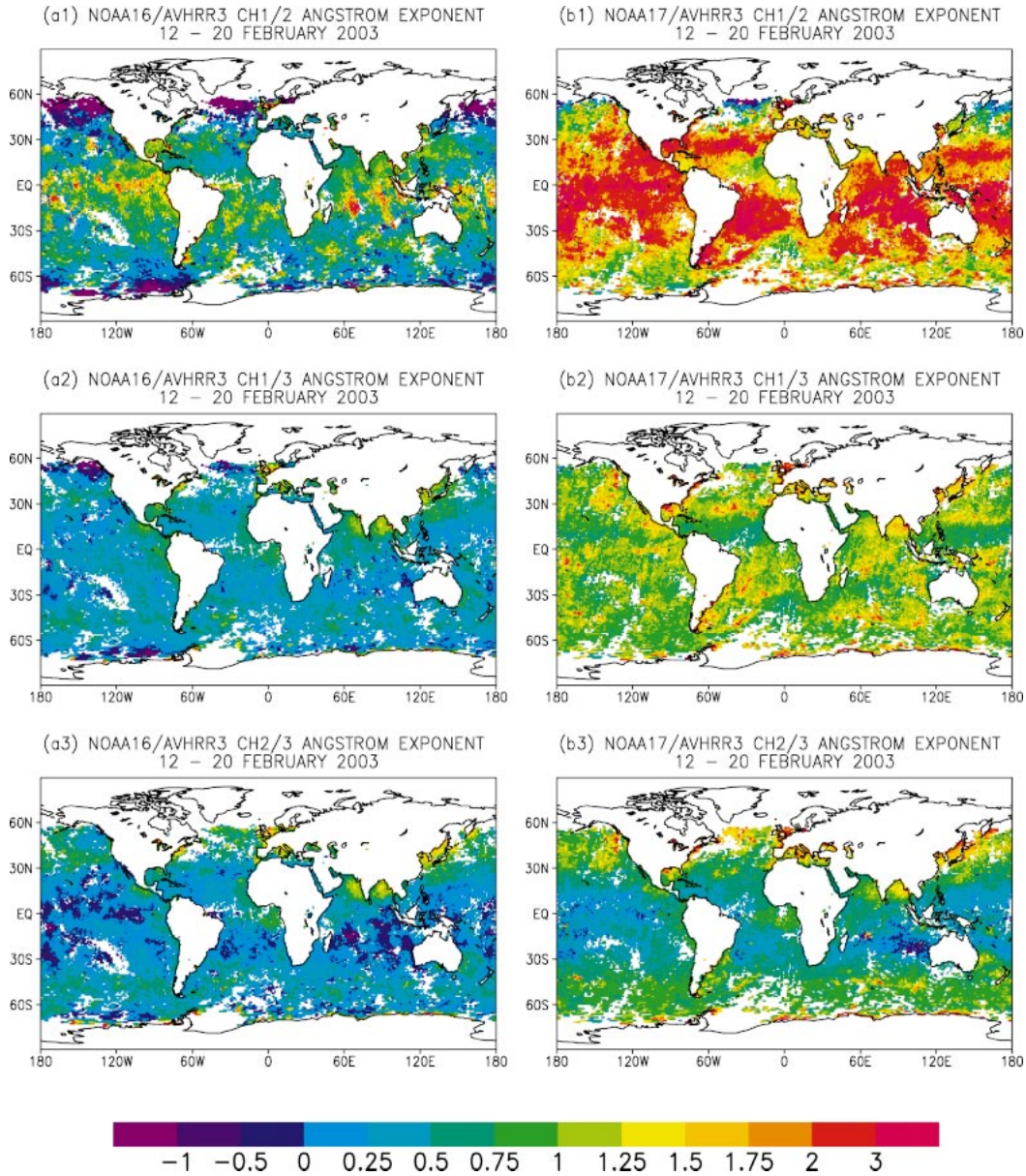


FIG. 11. Global distribution of the AE over oceans derived from different pairs of AVHRR/3 channels: 1) α_{12} , 2) α_{13} , and 3) α_{23} on board (a) *NOAA-16* and (b) *NOAA-17*. Note that each point on the map is an $[8 \text{ day} \times (1^\circ)^2]$ average.

From *NOAA-16*, the average AE parameters are in a reasonable range from all pairs of channels, $\alpha_m \sim 0.41\text{--}0.50$. The average *NOAA-17* AE calculated with the use of channel 3A (α_{13} and α_{23}), $\alpha_m \sim 0.70\text{--}1.17$, exhibits a high bias, whereas the average AE derived from channels 1 and 2, $\alpha_m \sim 2.3$, is clearly unrealistic. Recall that τ_1 from *NOAA-17* is biased with respect to *NOAA-16* by $\sim +3 \times 10^{-2}$, τ_2 by $\sim -1 \times 10^{-2}$, and τ_3 by -2×10^{-2} (cf. Figs. 5 and 10). Systematic positive and negative τ differences between given channels from the two platforms may result in significant biases in the

respective AEs. All empirical STDs in Fig. 12 exceed the expected natural variability in the AE ($\sigma_\alpha \sim 0.3$), indicating a significant contribution from α errors. In particular, the STDs are always higher for *NOAA-17* compared to *NOAA-16*, and in α_{12} compared to $\alpha_{13,23}$, suggesting that the magnitudes of the α errors are larger in the respective cases. Note that unscreened outliers may significantly affect the estimated STD and shape of the histograms (which deviate from Gaussian, in all cases). The α retrievals from *NOAA-16* are consistently closer to Gaussian shape than their *NOAA-17* counter-

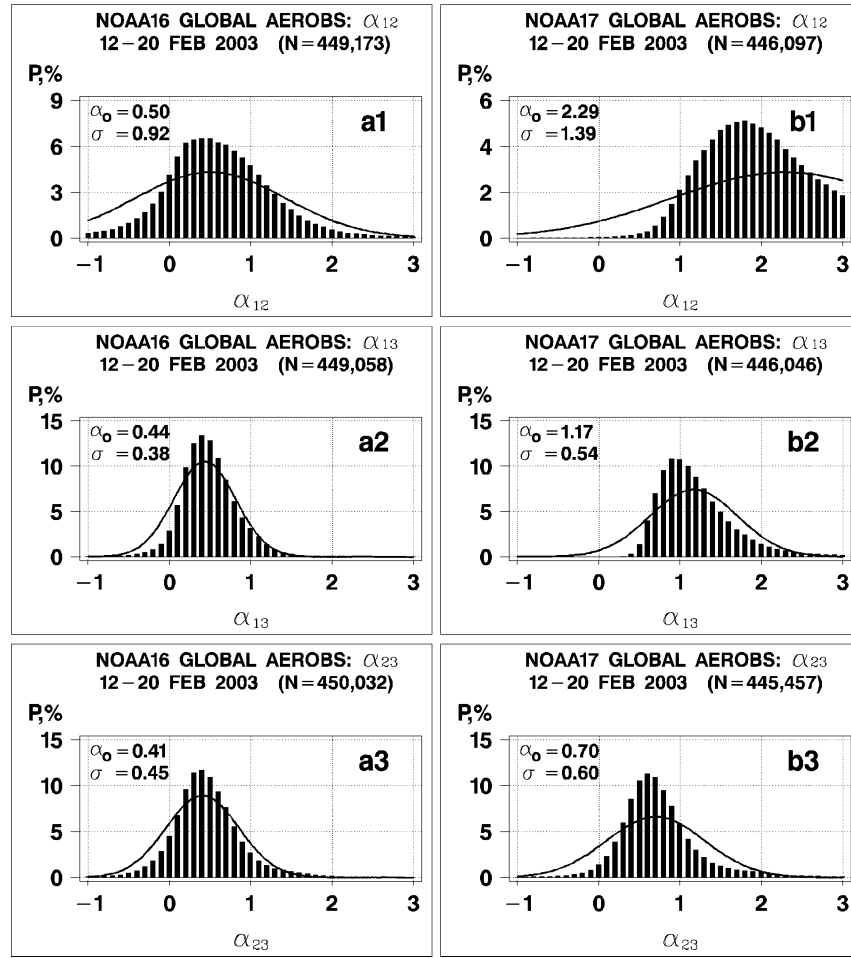


FIG. 12. Histograms (bars centered on $\Delta\alpha = 1 \times 10^{-1}$ bins) and their fit with normal PDFs (solid line) of the AEs, α , derived from different pairs of AVHRR/3 channels: 1) α_{12} , 2) α_{13} , and 3) α_{23} on board (a) NOAA-16 and (b) NOAA-17.

parts. From both platforms, α_{12} deviates most from Gaussian, because the spectral amplification factor between channels 1 and 2 is largest. The ensemble STDs, and degree of distortion, depend upon the channel-specific *systematic* and *random* τ errors, which, in turn, are amplified in inverse proportion to τ .

d. Scattergrams of α versus τ

Figure 13 show scattergrams of α versus τ_1 . Average $1/\tau$ trends and their respective equations are superimposed. The smallest trend is observed in α_{23} from NOAA-17. Note that this does not necessarily mean that systematic errors are zero in both τ_2 and τ_3 . The errors may simply have the same sign, and a coherent magnitude, causing them to approximately compensate for one another in Eq. (7). For the other five AEs, the α trends are significant (increasing with τ for NOAA-16, and decreasing for NOAA-17). All scattergrams reveal $1/\tau$ -type noise around the average trends, which are largest in α_{12} and smallest in α_{13} .

Two observations from Fig. 13 suggest that these features are more likely to be the result of data errors rather than real physics. First, for the same pair of channels, trends are dramatically different for the two platforms (even their signs are different). Second, the scatter appears to increase with the spectral amplification factor as Eq. (7) predicts: it is largest for α_{12} ($\Lambda_{12} \sim 3.627$) and smallest for α_{13} ($\Lambda_{13} \sim 1.066$).

e. Implications for implementation of a multichannel τ algorithm

The results of this section are fundamental for the strategy of future improvements to the operational AEROS product and, in particular, the possibility of switching to a dependent, multichannel algorithm (e.g., Higurashi and Nakajima 1999; Mishchenko et al. 1999). For the AVHRR spectral information (i.e., α) to improve the accuracy of τ retrievals, two conditions must be met: 1) the aerosol phase function in backscatter should be well predicted from α and 2) the accuracy of the pre-

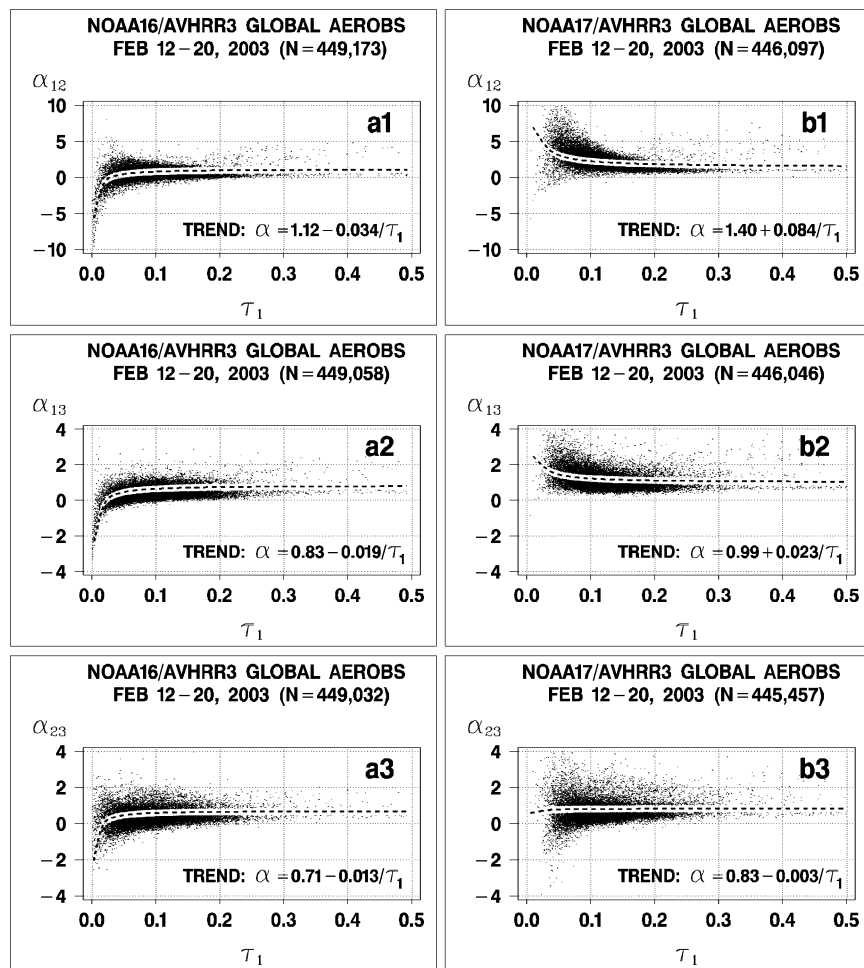


FIG. 13. Scattergrams of α_{ij} vs τ_1 : 1) $1(\lambda_1 = 0.63)/2(\lambda_2 = 0.83)$, α_{12} ; 2) $1(\lambda_1 = 0.63)/2(\lambda_3 = 1.61)$, α_{13} ; and 3) $2(\lambda_2 = 0.83)/3(\lambda_3 = 1.61)$, α_{23} , on board (a) *NOAA-16* and (b) *NOAA-17*. Average $1/\tau$ trends (dashed lines) and respective trend equations are superimposed.

dictor (i.e., α) should be better than its a priori uncertainty in order to reduce the a priori uncertainty in the predictant (phase function). Data presented in this section clearly show that in the operational NOAA practice, the a priori uncertainty in α cannot be reduced for typical oceanic conditions. As a result, the phase function predicted from the erroneous α will exceed the limits of its natural variability, leading to τ errors larger than those obtained from a globally averaged phase function. This implies that the single-channel algorithm is more robust and thus preferable to a dependent, multichannel simultaneous algorithm in the AEROS operations.

7. Discussion and conclusions

An improved and extended *third-generation* aerosol algorithm has been implemented at NOAA-NESDIS with the launch of the AVHRR/3 sensor on board the NOAA-KLM series of satellites. The operational aerosol product (AEROS) builds upon our past extensive ex-

perience from AVHRR/2 on board pre-KLM platforms. In particular, it continues to employ a single-channel retrieval methodology, where all oceanic and atmospheric parameters are fixed in the radiative transfer model with the exception of AOD.

The continued use of a single-channel methodology is deliberate, even while the current trend in the aerosol remote sensing community is to use multichannel algorithms to simultaneously estimate the aerosol size information (in our case, α) and τ at each retrieval point. This trend is quite understandable and justified given the availability of advanced aerosol sensors such as MODIS (Tanre et al. 1997). Greater care must be exercised, however, when channel data are used simultaneously from older sensor designs, such as the AVHRR (e.g., Mishchenko et al. 1999; Higurashi and Nakajima 1999; Geogdzhayev et al. 2002). Satellite measurements are influenced by two independent factors: 1) physical processes in the ocean and atmosphere that affect the radiation field, and 2) instrumental measure-

ment errors. An inversion must properly take into account both factors, not just the first of them. This fact is well known with regard to infrared remote sensing (e.g., Rogers 1976 and references therein), and likewise for aerosol inversions from the ground (e.g., Dubovik and King 2000), but it is often overlooked in aerosol remote sensing from space. It is particularly relevant for the AVHRR sensor, which was, in its conception, primarily meant to be an imager for cloud detection and weather analyses.

The relative contribution of the physical and instrumental errors is no doubt different for different sensors (e.g., MODIS versus AVHRR). In addition, it may also dramatically depend on the preprocessing used for channels from the same sensor (calibration, cloud screening, quality control, noise reduction). The latter differences suggest that there may never be a “universal” AVHRR aerosol retrieval algorithm. In some cases, neglecting instrumental factors may be more justified than in others. In particular, the above-mentioned analyses by Mishchenko et al. (1999), Higurashi and Nakajima (1999), Geogdzaeyev et al. (2002) are all based on the use of historical AVHRR data, in which many data issues are believed to have been mitigated. Ignatov and Nalli (2002) have argued, however, that even in the case of careful preprocessing (i.e., the historical PATMOS archive), instrumental factors cannot be neglected. In some cases, the instrumental factors may be at least as important, or even more important, as the physical factors.

The real-time AEROS processing is a clear example of when the uncertainty in AVHRR calibration is the major limiting factor of aerosol retrievals. The uncertainty in the aerosol microphysics, however important for the τ retrievals, cannot be narrowed down. Moreover, a dependent, multichannel methodology may well produce an even less accurate τ product. This is because the errors in the estimated α exceed the range of its natural variability. Fixing aerosol phase function at its global average value, while being an important limitation, provides more stability than predicting it from a noisy AE. The value of the single-channel aerosol product is twofold. First, it provides reliable assessment of spatiotemporal variability of the aerosol optical depth over global ocean, in real time. (Recall that the calibration errors lead only to a linear transformation of the AOD field as a whole.) Second, aerosol retrievals derived from low radiances are very sensitive to radiometric errors, therefore providing a valuable tool for identifying and monitoring the radiometric performance of the low gain of the *individual* AVHRR/3 reflectance channels.

It is thus recommended that the single channel retrieval methodology remain in place for the five IJPS platforms (NOAA-N and -N', and METOP-1, -2, and -3) that will carry the AVHRR/3 instrument, where reflectance channels are not calibrated on board. The operational AEROS AOD product will continue to be

available for downloading from the Satellite Active Archive Web site. One should keep in mind the qualitative real-time nature of this product, and care is advised during its quantitative analyses and use [e.g., for the aerosol correction for SST; Nalli and Stowe (2002)].

More sophisticated multichannel solutions may be tested with historical AVHRR data, where many data issues that were unavoidable in the real-time operational processing can be resolved. However, even for historical data, the provision of a single-channel product is advisable. This allows for testing the actual radiometric performance of the individual channels, as well as post-launch calibration, and finally it provides a benchmark aerosol product against which the multichannel improvements are to be evaluated. We emphasize that improvements to the nonaerosol parameters of the aerosol algorithm discussed above (more accurate surface reflectance, and gaseous scattering and absorption) should be addressed at the time since they are expected to be equally, if not more, important for aerosol retrievals under typical oceanic conditions than improvements of the aerosol microphysics.

Empirical analyses in this paper suggest that AVHRR/3 channel 3A greatly enhances the potential for aerosol remote sensing beyond that provided by channels 1 and 2. More studies are needed to explore this potential and estimate it quantitatively. It is believed that many of the data problems observed in this study can be significantly constrained by using a suite of statistical procedures similar to the ones tested in sections 5 and 6. After quality assurance, the information content of AVHRR/3 can be quantitatively addressed. At such time, more sophisticated multichannel retrievals will be tested. In particular, Tanre et al. (1996) suggest that reflectance measurements from space contain two to three pieces of aerosol information, which in principle may be captured with the three channels of AVHRR/3. These analyses are currently under way and their results will be reported elsewhere.

Acknowledgments. We are greatly indebted to Larry Stowe (retired) and Nagaraja Rao (deceased) who initiated the program in aerosol remote sensing applications from AVHRR at NOAA/NESDIS. We are grateful to Jim Coakley (Oregon State University) for stimulating discussions. Thanks go to Alexander Vassilkov (SSAI), and to NESDIS colleagues Bill Pichel, Levin Lauritson, Tom Schott, Gary Ellrod, and Al Strong for helpful comments and advice; to Yan Ming Wang, Emily Harrod, Alex Kidd, and Mike Simpson for help with the equator crossing time data; and to Changyong Cao, Jerry Sullivan, Andy Heidinger, and Fred Wu for assistance with and discussions of the AVHRR calibration. This work was funded under the Integrated Program Office (NOAA/NASA/DOD), NASA EOS/CERES (NASA Contract L-90987C), the Joint Center for Data Assimilation, and NOAA/NESDIS Ocean Remote Sensing programs. We are thankful to Steve Mango (IPO),

Fuzhong Weng (NOAA/NESDIS), and Bruce Wielicki (NASA LaRC) for their support and encouragement. In-depth constructive reviews by Lorrane Remer (NASA GSFC), and by two anonymous reviewers, helped us to bring the results of this study into a more adequate perspective, and also helped us present them more clearly. We would like to acknowledge Edward V. Browell and Joy Duke (NASA LaRC) for their excellent editorial work.

REFERENCES

- Cox, C., and W. Munk, 1954: Measurement of the roughness of the sea surface from photographs of the sun glitter. *J. Opt. Soc. Amer.*, **44**, 838–850.
- Dave, J. V., 1973: Development of the programs for computing characteristics of ultraviolet radiation: Scalar case. Tech. Rep. NASS-21680, NASA GSFC, Greenbelt, MD, 130 pp.
- Dubovik, O., and M. King, 2000: A flexible inversion algorithm for retrieval of aerosol optical properties from sun and sky radiance measurements. *J. Geophys. Res.*, **105**, 20 673–20 696.
- Geogdzhayev, I., M. Mishchenko, W. Rossow, B. Cairns, and A. Lacis, 2002: Global two-channel AVHRR retrievals of aerosol properties over ocean for the period of NOAA-9 and preliminary retrievals using NOAA-7 and NOAA-11 data. *J. Atmos. Sci.*, **59**, 262–278.
- Goodrum, G., K. Kidwell, and W. Winston, Eds., 2003: NOAA-KLM user's guide. NOAA/NESDIS, 1106 pp. [Available from National Climatic Data Center, 151 Patton Ave., Asheville, NC 28801-5001; also available online at <http://www2.ncdc.noaa.gov/docs/klm/index.htm>.]
- Heidinger, A. K., C. Cao, and J. Sullivan, 2002: Using Moderate Resolution Imaging Spectrometer (MODIS) to calibrate Advanced Very High Resolution Radiometer reflectance channels. *J. Geophys. Res.*, **107**, 4702, doi:10.1029/2001JD002035.
- Higurashi, A., and T. Nakajima, 1999: Development of a two-channel aerosol retrieval algorithm on a global scale using NOAA/AVHRR. *J. Atmos. Sci.*, **56**, 924–941.
- Husar, R., J. Prospero, and L. Stowe, 1997: Characterization of tropospheric aerosols over oceans with the NOAA AVHRR optical thickness operational product. *J. Geophys. Res.*, **102**, 16 889–16 909.
- Ignatov, A., 2002: Sensitivity and information content of aerosol retrievals from AVHRR: Radiometric factors. *Appl. Opt.*, **41**, 991–1011.
- , and L. Stowe, 2000: Physical basis, premises, and self-consistency checks of aerosol retrievals from TRMM VIRS. *J. Appl. Meteor.*, **39**, 2259–2277.
- , and N. Nalli, 2002: Aerosol retrievals from multiyear multi-satellite AVHRR Pathfinder Atmosphere (PATMOS) dataset for correcting remotely sensed sea surface temperatures. *J. Atmos. Oceanic Technol.*, **19**, 1986–2008.
- , and L. Stowe, 2002a: Aerosol retrievals from individual AVHRR channels. Part I: Retrieval algorithm, and transition from Dave to 6S radiative transfer model. *J. Atmos. Sci.*, **59**, 313–334.
- , and L. Stowe, 2002b: Aerosol retrievals from individual AVHRR channels. Part II: Quality control, probability distribution functions, and consistency checks of retrievals. *J. Atmos. Sci.*, **59**, 335–362.
- , S. Sakerin, and G. Korotaev, 1995: Validation of the NOAA/NESDIS satellite aerosol product over the North Atlantic in 1989. *J. Geophys. Res.*, **100**, 5123–5132.
- , —, and R. Singh, 1998: Sensitivity study of the Ångström exponent derived from AVHRR over oceans. *Adv. Space Res.*, **21**, 439–442.
- Kaufman, Y., B. Holben, D. Tanre, I. Slutsker, A. Smirnov, and T. Eck, 2000: Will aerosol measurements from Terra and Aqua polar orbiting satellites represent the daily aerosol abundance and properties? *Geophys. Res. Lett.*, **27**, 3861–3864.
- Kidwell, K., Ed., 1998: NOAA polar orbiter data user's guide (TIROS-N, NOAA-6, -7, -8, -9, -10, -11, -12, -13, and -14). NOAA/National Environmental Satellite, Data, and Information Service, 412 pp. [Available from National Climatic Data Center, 151 Patton Ave., Asheville, NC 28801-5001; also available online at <http://www2.ncdc.noaa.gov/docs/podug/index.htm>.]
- King, M., Y. Kaufman, D. Tanre, and T. Nakajima, 1999: Remote sensing of tropospheric aerosols from space: Past, present, and future. *Bull. Amer. Meteor. Soc.*, **80**, 2229–2259.
- McClain, P., 1989: Global SST and cloud clearing for aerosol optical depth estimates. *Int. J. Remote Sens.*, **10**, 763–769.
- , W. Pichel, and C. Walton, 1985: Comparative performance of AVHRR-based multi-channel sea surface temperatures. *J. Geophys. Res.*, **90**, 11 587–11 601.
- Mishchenko, M., I. Geogdzhayev, B. Cairns, W. Rossow, and A. Lacis, 1999: Aerosol retrievals over the oceans by use of channels 1 and 2 AVHRR data: Sensitivity analysis and preliminary results. *Appl. Opt.*, **38**, 7325–7341.
- Myhre, G., and Coauthors, 2004: Intercomparison of satellite retrieved aerosol optical depth over the ocean. *J. Atmos. Sci.*, in press.
- Nalli, N., and L. Stowe, 2002: Aerosol correction for remotely sensed sea surface temperature from the NOAA AVHRR. *J. Geophys. Res.*, **107**, 3172, doi:10.1029/2001JC00162.
- O'Neill, N., A. Ignatov, B. Holben, and T. Eck, 2000: The log-normal distribution as a reference for reporting aerosol optical depth statistics: Empirical tests using multi-year, multi-site AERONET sun photometer data. *Geophys. Res. Lett.*, **27**, 3333–3336.
- Rao, N., and J. Chen, 1996: Post-launch calibration of the visible and near-IR channels of the Advanced Very High Resolution Radiometer (AVHRR) on the NOAA-14 spacecraft. *Int. J. Remote Sens.*, **17**, 2743–2747.
- , and —, 1999: Revised post-launch calibration of the visible and near-IR channels of the Advanced Very High Resolution Radiometer (AVHRR) on the NOAA-14 spacecraft. *Int. J. Remote Sens.*, **20**, 3485–3491.
- , L. Stowe, and P. McClain, 1989: Remote sensing of aerosols over oceans using AVHRR data: Theory, practice and applications. *Int. J. Remote Sens.*, **10**, 743–749.
- Rao, P. K., S. J. Holmes, R. K. Anderson, J. S. Winston, and P. E. Lehr, Eds., 1990: *Weather Satellites: Systems, Data and Environmental Applications*. Amer. Meteor. Soc., 503 pp.
- Remer, L., and Coauthors, 2002: Validation of MODIS aerosol retrieval over ocean. *Geophys. Res. Lett.*, **29**, 8008, doi:10.1029/2001GL013204.
- Rogers, C. D., 1976: Retrieval of atmospheric temperature and composition from remote measurements of thermal radiation. *Rev. Geophys. Space Phys.*, **14**, 609–624.
- Rossow, W., and R. Shiffer, 1999: Advances in understanding clouds from ISCCP. *Bull. Amer. Meteor. Soc.*, **80**, 2261–2287.
- Smirnov, A., B. Holben, Y. Kaufman, O. Dubovik, T. Eck, I. Slutsker, C. Pietras, and R. Halthore, 2002: Optical properties of atmospheric aerosol in maritime environments. *J. Atmos. Sci.*, **59**, 501–523.
- Stowe, L., A. Ignatov, and R. Singh, 1997: Development, validation and potential enhancements to the second generation operational aerosol product at NOAA/NESDIS. *J. Geophys. Res.*, **102**, 16 923–16 934.
- , H. Jacobowitz, G. Ohring, K. Knapp, and N. Nalli, 2002: The Advanced Very High Resolution Radiometer Pathfinder Atmosphere (PATMOS) climate dataset: Initial analyses and evaluations. *J. Climate*, **15**, 1243–1260.
- Su, W., T. Charlock, and K. Rutledge, 2002: Observations of reflectance distribution around sunglint from a coastal oceanic platform. *Appl. Opt.*, **41**, 7369–7383.
- Tahnk, W., and J. Coakley, 2001a: Improved calibration coefficients for NOAA-14 AVHRR visible and near-IR channels. *Int. J. Remote Sens.*, **22**, 1269–1283.
- , and —, 2001b: Updated calibration coefficients for NOAA-

- 14 AVHRR channels 1 and 2. *Int. J. Remote Sens.*, **22**, 3053–3057.
- Tanre, D., M. Herman, and Y. Kaufman, 1996: Information on aerosol size distribution contained in solar reflected spectral radiances. *J. Geophys. Res.*, **101**, 19 043–19 060.
- , Y. Kaufman, M. Herman, and S. Mattoo, 1997: Remote sensing of aerosol properties over oceans using the MODIS/EOS spectral radiances. *J. Geophys. Res.*, **102**, 16 971–16 989.
- Vermote, E., D. Tanre, J. L. Deuze, M. Herman, and J. J. Morcrette, 1997: Second Simulation of the Satellite Signal in the Solar Spectrum, '6S': An overview. *IEEE Trans. Geosci. Remote Sens.*, **35**, 675–686.
- Wagner, R., S. Nemesure, and S. Schwartz, 1997: Aerosol optical depth over oceans: High space- and time-resolution retrieval and error budget from satellite radiometry. *J. Atmos. Oceanic Technol.*, **14**, 577–590.
- Walton, C., W. Pichel, J. Sapper, and D. May, 1998: The development and operational application of nonlinear algorithms for the measurement of sea surface temperatures with the NOAA polar orbiting environmental satellites. *J. Geophys. Res.*, **103**, 27 999–28 012.
- Weinreb, M., M. Jamieson, N. Fulton, Y. Chen, J. Johnson, J. Bremer, C. Smith, and J. Baucom, 1997: Operational calibration of GOES-8 and -9 imagers and sounders. *Appl. Opt.*, **27**, 6895–6904.